Empirical Relationship Between the Doppler Centroid Derived From X-Band Spaceborne InSAR Data and Wind Vectors

Citation for the original published paper (version of record):
Elyouncha, A., Eriksson, L., Romeiser, R. et al (2022). Empirical Relationship Between the Doppler Centroid Derived From X-Band Spaceborne InSAR Data
and Wind Vectors. IEEE Transactions on Geoscience and Remote Sensing, 60.
http://dx.doi.org/10.1109/TGRS.2021.3066106

Empirical Relationship Between the Doppler Centroid Derived From X-Band Spaceborne InSAR Data and Wind Vectors

Anis Elyouncha, *Member, IEEE*, Leif E. B. Eriksson, *Member, IEEE*, Roland Romeiser, *Senior Member, IEEE*, and Lars M. H. Ulander, *Fellow, IEEE*

***Abstract*— One of the challenges in ocean surface current retrieval from synthetic aperture radar (SAR) data is the estimation and removal of the wave-induced Doppler centroid (DC). This article demonstrates empirically the relationship between the dc derived from spaceborne X-band InSAR data and the ocean surface wind and waves. In this study, we analyzed over 300 TanDEM-X image pairs. It is found that the general characteristics of the estimated dc follow the theoretically expected variation with incidence angle, wind speed, and wind direction. An empirical geophysical model function (GMF) is fit to the estimated dc and compared to existing models and previous experiments. Our GMF is in good agreement (within 0.2 m/s) with other models and data sets. It is found that the wind-induced Doppler velocity contributes to the total Doppler velocity with about 15% of the radial wind speed. This is much larger than the sum of the contributions from the Bragg waves (∼0.2 m/s) and the wind-induced drift current (∼3% of wind speed). This indicates a significant (dominant) contribution of the long wind waves to the SAR dc. Moreover, analysis of dual-polarized data shows that the backscatter polarization ratio (PR $= \sigma^0_{VV}/\sigma^0_{HH}$) and the dc polarization difference (PD $= |dc_{VV}| - |dc_{HH}|$) are systematically larger than 1 and smaller than 0 Hz, respectively, and both increase in magnitude with incidence angle. The estimated PR and PD are compared to other theoretical and empirical models. The Bragg scattering theory-based (pure Bragg and composite surface) models overestimate both PR and PD, suggesting that other scattering mechanisms, e.g., wave breaking, are involved. In general, it is found that empirical models are more consistent with both backscatter and Doppler data than theory-based models. This motivates a further improvement of SAR dc GMFs.**

***Index Terms*— Along-track interferometry (ATI), Doppler centroid (DC), Doppler oceanography, ocean surface winds, ocean surface currents, synthetic aperture radar (SAR), TanDEM-X.**

I. Introduction

SYNTHETIC aperture radar (SAR) has been established as a vital component of ocean remote sensing systems. Owing to its high spatial resolution, SAR is particularly useful for studies involving small-scale circulation in coastal areas, estuaries, and shelf seas. Since SAR provides complex data (magnitude and phase) and it tracks coherently the phase between consecutive pulses over the illumination time, its response is sensitive to both the roughness and the motion of the illuminated surface. Whilst improvements are on-going, SAR has been used for wind speed retrieval, e.g., [1] and directional swell spectra, e.g., [2] for many years. Recently, there has been growing interest in ocean surface current retrievals as an additional SAR-derived product. In order to infer ocean surface currents from SAR Doppler data, the wave contribution needs to be accurately estimated and removed from the measured Doppler centroid (DC). This task is one of the main challenges in current retrieval from SAR. It requires an accurate Doppler model, i.e., a model that predicts the dc measured by SAR in the absence of ocean currents.

Although measurement of ocean surface currents was first demonstrated in 1987 [3] using interferometric SAR (InSAR), the contribution of waves to the measurements was not accounted for. In the Loch Linnhe experiment [4], deviations between InSAR-derived and *in situ*-measured horizontal velocities were observed. These deviations were explained as effects of wave motions, i.e., modulation of the short Bragg waves by the current in addition to contributions of orbital motions of longwaves. Based on analysis of the C-band ENVISAT/advanced SAR (ASAR) data on the global scale, [5], [6] have shown that the DC anomaly, i.e., the difference between the measured DC and the geometric Doppler shift carries a clear geophysical signature. The authors showed that this signature is correlated with the global atmospheric circulation (wind field). Furthermore, [7] suggested the use of this Doppler anomaly for wind retrieval.

Moreover, it has been found (e.g., [8]) that the accuracy of sea surface currents retrieval is highly dependent on the accuracy with which the wave contribution (also called wave bias) is estimated and removed from the total measured velocity. This step requires accurate wind and wave information and a model relating the wave parameters (or wind vectors as a proxy) to the DC measured by SAR.

The dc is defined as the power-weighted mean frequency of the power spectrum of the backscattered signal. This includes the satellite motion relative to the solid rotating Earth and the motion of the surface. Theoretically, there are three different

Manuscript received May 16, 2020; revised October 17, 2020 and February 14, 2021; accepted February 27, 2021. This work was supported by the Swedish National Space Agency under Contract dnr 167/14 and Contract dnr 214/19. *(Corresponding author: Anis Elyouncha.)*

Anis Elyouncha, Leif E. B. Eriksson, and Lars M. H. Ulander are with the Department of Space, Earth and Environment, Chalmers University of Technology, 41296 Gothenburg, Sweden (e-mail: anis.elyouncha@chalmers.se; leif.eriksson@chalmers.se; lars.ulander@chalmers.se).

Roland Romeiser is with the Department of Ocean Sciences, Rosenstiel School of Marine and Atmospheric Science, University of Miami, Miami, FL 33149 USA (e-mail: rromeiser@rsmas.miami.edu).

Color versions of one or more figures in this article are available at https://doi.org/10.1109/TGRS.2021.3066106.

Digital Object Identifier 10.1109/TGRS.2021.3066106

approaches to simulate the DC from the sea surface. These are listed in the following in order of increasing computational efficiency.

The first approach is based on a numerical solution (using for instance the method of moments) of Maxwell's equations [9]. It consists of generating realizations of surface elevation from a given wave height spectrum (e.g., Pierson-Moskowitz spectrum) and solving for the backscattered field. This procedure is repeated for a number of time-evolving surface realizations and the statistical average is computed. The time evolution is based on the wave dispersion relation. This approach is considered the most accurate and often used as a reference to validate theoretical models, but it is the most expensive computationally.

The second approach [10]–[13] consists in using the spatio-temporal autocovariance of the scattered field derived from a theoretical model, e.g., Kirchhoff approximation (KA) and small slope approximation (SSA). As in the first approach, the time dependence of the autocovariance function is based on the wave dispersion relation. The dc can either be derived as the first moment of the Doppler spectrum, which is the Fourier transform of the autocovariance, or directly as the time derivative of the autocovariance function at $t = 0$.

The third approach is using the modulation transfer function (MTF) [14], i.e., assuming that the backscatter modulation is small and linearly related to the sea surface wave slopes. This approach is discussed in [5], [15]–[17] and more recently in [18] and [19]. This approach is the most efficient computationally [15], and it was shown to be comparable to numerical simulations (e.g., [15], [20]). The Doppler model based on this approach requires an accurate normalized radar cross section (NRCS) model. For instance, the Doppler model in [15] is based on the improved composite surface model developed in [21] and the Doppler model, called DopRIM, in [16] and [17] is based on the semi-empirical model developed in [22] which is also based on the composite surface model but includes the wave breaking effect.

The estimation of the wave-induced dc based on the radar MTF concept is described in more detail in Sections II-B and II-C. The radar MTF is composed of geometric and hydrodynamic components. Several authors [23]–[26] have investigated and measured the radar MTF and also compared their data to theoretical models. The results of these studies sometimes disagree or even contradict the theory. Though they often roughly agree on the functional form, large discrepancies are still reported and remain unexplained.

The discrepancy between different studies is mainly due to the hydrodynamic MTF which was first derived in [27] and [28]. Then, other authors suggested the important role of the wind stress modulation by the longwaves [23], [25] and the role of the intermediate waves [26], [29]. Even by including the intermediate waves and wind modulation effect, it was, for instance, found [26] that the theoretical hydrodynamic MTF still underestimates the measured MTF particularly at high microwave frequencies (C- and X-band). [30] suggested the effect of scattering from bound waves in addition to free Bragg waves. The author showed that including this effect explains the higher mean Doppler frequencies in horizontal horizontal (HH) than vertical vertical (VV). In addition, [22], [31] suggested the effect of wave breaking and parasitic capillary waves on the NRCS model and consequently on the MTF. The authors showed that including these effects in the MTF reduces the discrepancy between the models and the data.

Alternatively, the SAR dc can be modeled empirically by matching collocated (in space and time) pairs of wind vectors (or wave parameters) and the measured Doppler frequency shift. The underlying assumption is that contributions to dc that are uncorrelated to wind average out. This is the approach followed in this article. Most of the previous studies are either airborne or tower-based. Only a few studies, e.g., [5], [7] using the C-band ENVISAT/ASAR data, have investigated the empirical relationship between spaceborne SAR dc and ocean surface wind vectors. More recent studies used an airborne Doppler scatterometer [18] and a sea platform-based scatterometer in the Black Sea [19] both operating at Ka-band. To our knowledge, no spaceborne X-band SAR study showing such a relationship has been published yet.

In this article, we demonstrate the empirical relationship between the dc derived from spaceborne X-band InSAR data acquired by the TanDEM-X mission and the ocean surface wind. The empirical relationship, at two different polarizations, HH and VV, is compared to existing MTF-based and empirical Doppler models. Moreover, we analyzed dual-polarized data and compared the estimated NRCS polarization ratio (PR) and dc polarization difference (PD) to existing theoretical and empirical models.

II. Theoretical Background

A. DC Estimation (DCA and ATI)

The two common techniques used to estimate the dc from SAR data are Doppler centroid analysis (DCA) and along-track interferometry (ATI). In DCA, the geophysical dc (Doppler anomaly) is calculated as the difference between the total measured dc and the calculated geometric dc. The geometric dc is the Doppler shift due to the relative motion of the satellite and the solid rotating Earth and is calculated from known orbit parameters and attitude. The total dc is estimated from a single SAR image using two different approaches. The first approach is the spectral processing through the fast Fourier transform of the complex signal in the azimuth direction. The second approach is the so-called pulse-pair method or covariance method, which is based on approximating the first spectral moment (dc) using the phase difference between successive pulses [32].

One of the main challenges in the DCA method is the accurate calculation of the geometric dc [33]. The radar measures the power-weighted velocities of the scatterers within a resolution cell. The dc is the center frequency of the passage of a point scatterer through the antenna beam. Thus, if the antenna boresight is not pointing toward the point on the ground that is in the zero Doppler plane and this is not taken into account in the calculation of the geometric dc, the estimated Doppler spectrum will be shifted from zero. This would be interpreted as a velocity bias.

ATI is also affected by the geometric dc. There are two effects that can cause a nonzero geometric dc in ATI [34]. The first effect is due to satellite orbits convergence, i.e., nonparallel orbits with slowly changing InSAR baseline during data acquisition. The second effect is due to different antenna squint angles, i.e., the angle between the satellite velocity vector and the look vector of the antenna beam. Both effects induce shifted image spectra. The azimuth (common band) filtering is performed to remove the nonoverlapping parts of the azimuth image spectra. This mitigates the difference in DCs between the two SAR images. In the case of nonzero across-track baseline, the phase component due to topography needs to be removed. This step is also based on orbital parameters which are subject to errors. In practice, this is not accurate enough, thus both DCA and ATI methods require calibration.

The radial (horizontal) velocity measured using SAR (ATI and DCA) is calculated as

$$U_D = \frac{\pi f_{\rm dc}}{k_e \sin\theta} \approx \frac{\phi_{\rm int}}{2k_e \tau \sin\theta} \tag{1}$$

where k_e is the electromagnetic wavenumber, θ is the incidence angle, τ is the temporal baseline, $\phi_{\rm int}$ is the interferometric phase, and $f_{\rm dc}$ is the Doppler anomaly.

Note that 1 assumes that the vertical velocity component is negligible. In fact, this relationship between U_D, $\phi_{\rm int}$ and $f_{\rm DC}$ applies to all Doppler-based radar techniques (SAR and Doppler scatterometer, space-, air- or tower-borne). All these techniques differ mainly in how the phase $\phi_{\rm int}$ is estimated from the data. In Doppler scatterometry [18], for instance, $\phi_{\rm int}$ is the phase difference between consecutive pulses (called pulse-pairs), hence the temporal baseline is one pulse repetition interval (PRI). In ATI, $\phi_{\rm int}$ is the pixel-to-pixel phase difference between two coregistered complex SAR images separated in time by the temporal baseline τ. It can be shown [4], [35] that for small τ, the dc estimated from the interferometric phase is equivalent to the dc estimated from the Doppler spectrum, i.e., $\phi_{\rm int} \approx 2\pi f_{\rm DC} \tau$.

B. Modulation Transfer Function

According to the pure Bragg scattering theory [36], [37], the normalized radar cross section (NRCS or σ^0) of the ocean surface is proportional to the wave height spectral density, i.e., $\sigma^0 = T^0_{pp}(\theta, k_e, \epsilon_r)\Psi(k_B, \varphi)$, evaluated at the Bragg wavenumber ($k_B = 2k_e \sin\theta$). The coefficient T (thus also σ^0) depends on the radar frequency, polarization pp, incidence angle, azimuth angle φ, and dielectric constant ϵ_r. In the presence of longwaves (waves several times longer than the Bragg wave), the slopes of these waves will modify the incidence angle (thus also k_B). Taking this into account leads to the composite surface model (also called the two-scale model) [37], [38], in which, the NRCS depends also on the slope of the modulating longwave.

The concept of MTF was introduced and described in several articles [14], [27], [28], [39]. It is based on the assumption that fluctuations in the backscattered power due to longwaves are linearly related to the longwaves slopes. Under this assumption, the NRCS can be decomposed into a mean $\overline{\sigma}^0$ and a fluctuating component $\tilde{\sigma}^0$. The fluctuating component is described by the product of the dimensionless MTF and the slope of the modulating longwaves.

As will be shown later, the MTF plays a crucial role in the Doppler model. It has been studied theoretically and experimentally by many authors, e.g., [23], [40], [41]. The MTF can be derived theoretically [39], semi-empirically [31] or empirically [24], [42], [43]. The different components of the MTF are discussed in more detail in Sections II-B-1–3.

1) Range MTF: The height of longwaves modulates the NRCS by changing the distance between the radar antenna and the surface. The slope of these waves changes the effective illuminated area. The first effect is given by [14] ($M^{\rm rg} = 3\tanh(kD)/kH$), where H is the altitude of the radar antenna and D the water depth, hence it is negligible for spaceborne systems. The second effect, called range bunching, is however not negligible [44]. It is approximated, for a pulse limited radar, by [14] $M^{\rm rb}(\theta, \varphi) = i\cot\theta\cos\varphi$. where i is the imaginary unit and φ is the direction of the long modulating wave with respect to radar look direction.

2) Tilt MTF: The tilt modulation is due to the variation of the NRCS which is due to change in the local incidence angles through the slopes of the long modulating waves. Thus, it strongly depends on the backscattering model which dictates its variation with incidence angle. The tilt MTF can be estimated from a theoretical or empirical backscatter model. Its expression is given in Appendix B. For illustration, the tilt MTF has been simulated from different NRCS models.

Fig. 1 shows the tilt MTF simulated from the pure Bragg scattering model, the composite surface model (assuming Phillips spectrum [45], see Appendix D), the empirical X-band geophysical model function (GMF) XMOD2 [46] and the C-band GMF CMOD5 [47]. It can be observed that the four models agree qualitatively in their variation with incidence angle. They also agree on the fact that the MTF is larger in HH than VV and that the PR increases with incidence angle. However, large differences (up to ~4 dB) are found between different models, which will (as shown later) induce differences in the simulated Doppler velocity. The relatively large differences between CMOD5 and XMOD2 are partially due to frequency difference (5.3 GHz versus 9.65 GHz) and partially due to inherited biases from the data sets used to construct each GMF. CMOD5 was built using European Remote Sensing Satellite (ERS)-2/active microwave instrument (AMI) scatterometer data [47] and XMOD2 was built using TerraSAR-X SAR data [46]. Thus, in addition to frequency difference, these two sensors differ in spatial resolution and calibration.

3) Hydrodynamic MTF: The basic concept of the hydrodynamic MTF is the variation of the Bragg waves amplitude along the long modulating waves by straining [27], [28]. There are additional contributions, such as effects of wind stress variations along the modulating wave and effects of wave breaking [25], [31]. The expression of the Bragg hydrodynamic MTF can be found in [28], [39], [48], and [15] (see also Appendix C) and the expression including other effects is given in [31].

The hydrodynamic MTF depends mainly on the wave spectrum, on the group and phase speed of the modulated waves and the relaxation rate β (see Appendix C). The main cause

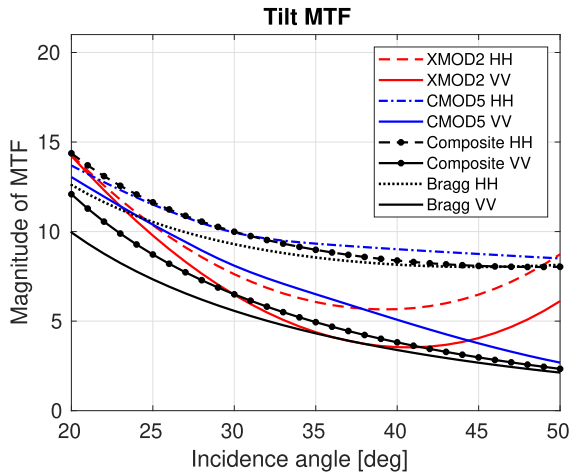

Fig. 1. Tilt MTF as a function of incidence angle, derived from different NRCS models (see legend), at $U_{10} = 7$ m/s (U_{10} is wind speed at 10 m height), upwave ($\varphi = 0°$).

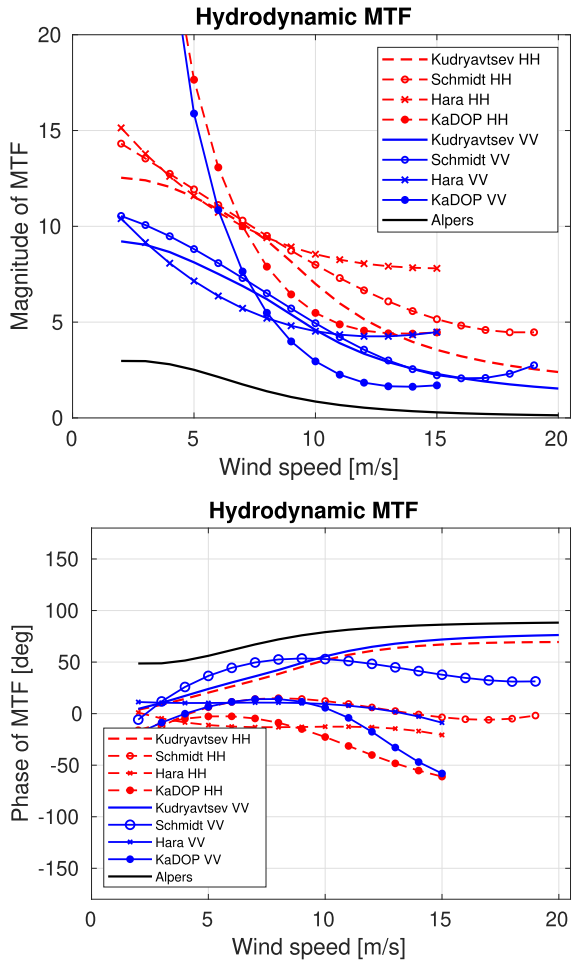

Fig. 2. Hydrodynamic MTF, upper panel: magnitude, lower panel: phase, from different models and experiments (see legend), at X-band, $\theta = 45°$, $f = \omega/2\pi = 0.15$ Hz, upwave ($\varphi = 0°$).

of the discrepancy between different models is the scattering mechanisms taken into account (e.g., Bragg, specular, wave breaking) and the relaxation rate. The relaxation rate is usually modeled as $\beta = \alpha(u_*/c)^n$, where u_* is the friction velocity and c is the wave phase velocity. Different studies report different coefficients α and n. Several parameterizations of the relaxation rate are discussed in [49], they all follow roughly similar behavior with wavenumber and wind speed but differ by an order of magnitude. One of the most commonly used parameterizations for gravity-capillary wind-waves is given in [50].

We have simulated the hydrodynamic MTF given by Alpers *et al.* [39] (using the relaxation rate given in [50]) and the hydrodynamic MTF suggested by Kudryavtsev *et al.* [31]. Note that the hydrodynamic MTF by Alpers *et al.* considers only the straining of Bragg waves by longwaves, while the MTF by Kuryavtsev *et al.* includes the wave breaking effect. In our implementation, the wind stress modulation is neglected. The latter effect becomes significant at high wind speeds ($U_{10} \gtrapprox 10$ m/s) [31]. We have also fit a third-order polynomial to the experimental MTFs by Hara and Plant [25] and Schmidt *et al.* [51]. Note that these two experimental results are obtained by subtracting the theoretical range and tilt MTFs from the measured total MTF. So, these so-called residual MTFs should contain the hydrodynamic MTF and other possible components. For comparison, the Ka-band empirical MTF by [43] is also plotted after subtracting the range and composite model tilt MTF.

Fig. 2 shows the result of the simulation for the magnitude (upper panel) and phase (lower panel). Generally, all the MTFs follow similar behavior, i.e., the magnitude decreases with increasing wind speed. However, differences up to ∼4 dB in magnitude and up to 90° in phase are observed. Note that the Bragg-theory-based model by Alpers *et al.* [39] is independent of polarization, while the model by Kudryavtsev *et al.* [31] and the experimental MTFs give higher magnitude at HH than VV. Moreover, Alpers' model is significantly lower in magnitude and higher in phase than the other models. Finally, KaDOP gives a significantly higher magnitude at low-to-moderate wind speeds ($U_{10} \lesssim 6$ m/s). This might be due to the large frequency difference between X-band and Ka-band.

C. Wave-Induced Doppler Velocity

1) Doppler Velocity Components: The radar measures the total relative velocity of the sea surface projected on the line of sight (LOS). This total velocity can be decomposed into three components

$$U_{\text{tot}} = U_{\text{geo}} + U_{\text{nwd}} + U_{\text{wd}}. \tag{2}$$

The first component (U_{geo}) is due to the motion of the radar platform relative to the solid rotating Earth [33], [52]. It involves the platform velocity, attitude, and antenna pointing. This term is independent of ocean motion.

The second component is the nonwind driven motion (U_{nwd}), which includes geostrophic currents (barotropic and baroclinic), tidal currents, and inertial oscillations. All these currents are induced by forces independent of the local wind and wind-waves.

The third component is the wind-driven component ($U_{\text{wd}} = U_E + U_S + U_{\text{wv}}$), which includes Ekman current induced by the local wind stress at the surface, the Stokes drift and wind-waves induced motion. The term U_{wv} does not represent

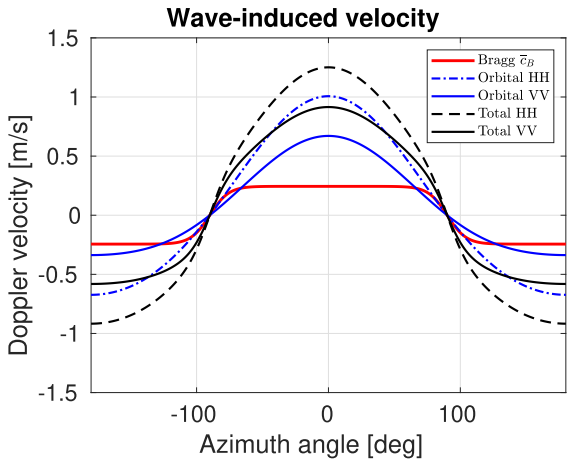

Fig. 3. Wave-induced Doppler velocity (5) simulated with the Bragg tilt and hydrodynamic MTF, $U_{10} = 7$ m/s, $\theta = 30°$, $H_s = 0.22U_{10}^2/g$, $A = H_s/2$, $w = 0.83g/U_{10}$.

an actual water mass transport (current) but it induces a Doppler shift in the radar measurements. It includes the Bragg wave phase speed and the correlation between the variation of the backscatter and the longwaves orbital velocities, and writes [15], [16]

$$U_{\rm wv} = \overline{c}_B + \frac{\langle U_o \sigma \rangle}{\langle \sigma \rangle} \tag{3}$$

where $\overline{c}_B$ is the weighted mean of the phase speed of the Bragg waves moving away and toward the radar and the weights are defined by a spreading function of the wave spectrum [53]. U_o is the LOS projection of the wave orbital velocity, $\langle \ldots \rangle$ denotes the average in space and time and σ is the local backscatter within the SAR resolution cell and during the SAR integration time.

It is of high importance to estimate $U_{\rm wv}$ accurately. This affects all measurement techniques and sensors: SAR, Doppler scatterometer [18], airborne, spaceborne, and tower-based [19] radars. The $U_{\rm wv}$ component was investigated by several authors [5], [10], [11], [15]–[17], [53], [54]. For instance, [10] showed that not only the width of the Doppler spectra broadens due to the motion of the longwaves, but also produces a shift in the centroid from the Bragg frequency. The author also showed that this shift is largest at lower incidence angles and higher radar frequencies. This means that even in the absence of currents, the radar would measure a dc shifted from the Bragg phase speed. It was also found [5] that this dc shift contributes a significant amount ($\sim$30% of the wind speed) to the Doppler velocity measured by SAR, and this contribution is often larger than the current we want to retrieve.

The sum of Ekman and Stokes components is sometimes called the "drift current", which is often parameterized in the wind speed. This was investigated and discussed in [55] and [56]. The reported values of the magnitude vary between $\sim$1% and $\sim$4% of the wind speed and direction between 0° and 45°. These values depend on the wind speed, fetch, sea state, and stratification.

2) Wave-Induced Doppler Model: In this section, we follow the MTF-based Doppler models in [5], [15]–[17]. It is shown in Appendix A that these models are equivalent. The general formula for the wave-induced Doppler velocity can be expressed as (see Appendix A for detailed derivation)

$$U_{\rm wv} = \overline{c}_B + \iint \left[\left[\left(M_0^r - M_0^t\right)\cot\theta + M_1^h\right]\cos\varphi + M_2^h \cot\theta\right] \cdot \omega(k) k \Psi(k,\varphi) k dk d\varphi \tag{4}$$

where $M^h = M_1^h + i M_2^h$ is the complex hydrodynamic MTF, $M_0^r = |M^{rb}(\theta,0)|$ and $M_0^t = |M^t(\theta,0)|$, $\Psi(k,\varphi)$ is the directional wave spectrum, φ is the angle between the radar look direction and the longwave direction.

The key factor in the Doppler model above is the knowledge of the MTFs and the directional wave spectrum Ψ. The main differences between the different Doppler models reside in using different scattering models, wave spectra, tilt, and hydrodynamic MTF and bounds of the integration.

For illustration, the above model is simplified to the case of one monochromatic longwave which gives

$$U_{\rm wv} = \overline{c}_B + \frac{\omega k A^2}{2} \cdot \left[\left[\left(M_0^r - M_0^t\right)\cot\theta + M_1^h\right]\cos\varphi + M_2^h \cot\theta\right]. \tag{5}$$

The term $\omega k A^2$ is equal to the surface Stokes drift magnitude U_S in deep water [5]. Thus, $U_{\rm wv}$ can either be calculated using the integrated wave parameters or the Stokes estimated from a wave model.

Fig. 3 shows $\overline{c}_B$ and $U_{\rm wv}$ as a function of relative wind direction for HH and VV polarizations, simulated from 5, using the Bragg tilt and hydrodynamic MTFs. It can be observed that the velocity due to the longwaves orbital velocities (second term of 5, blue curve) is significantly larger than the Bragg wave phase speed (first term of 5, red curve). It is also larger than the wind-induced drift current ($\approx 0.03 \cdot U_{10}$). The velocity varies sinusoidally with relative wind direction being highest positive in up-wind, lowest negative in the downwind, and vanishes in the crosswind direction. Note, also the slight upwind/downwind asymmetry. Finally, the simulation shows that $U_{\rm wv}$ at HH polarization is larger than $U_{\rm wv}$ at VV, which is due to the MTF (see Figs. 1 and 2).

3) Effect of the MTF on U_{wv}: In order to investigate the effect of the MTF on $U_{\rm wv}$ as a function of incidence angle, wind speed, and wind direction. we have simulated $U_{\rm wv}$ from 5 with different tilt MTFs (Bragg, XMOD2 and CMOD5). The simulation is performed for VV and HH. To convert the two GMFs from VV to HH, the PR in [57] and [58] were used for CMOD5 and XMOD2, respectively. Fig. 4 shows that all the velocity curves decrease with incidence angle (left panel), increase with wind speed (middle panel) and vary sinusoidally with relative wind direction (right panel). All the models agree on the fact that $U_{\rm wv}$ at HH is higher than at VV and that the PD increases with incidence angle and wind speed. However, the PD is very different in both absolute value and increase rate, being much larger using the theoretical Bragg model than the empirical GMFs. The discrepancy between different models varies with incidence angle, wind speed, and direction and reaches up to 0.5 m/s. This is of the same order of magnitude as many ocean surface currents.

The results of the simulations above show how difficult it is to estimate the wave-induced Doppler velocity using

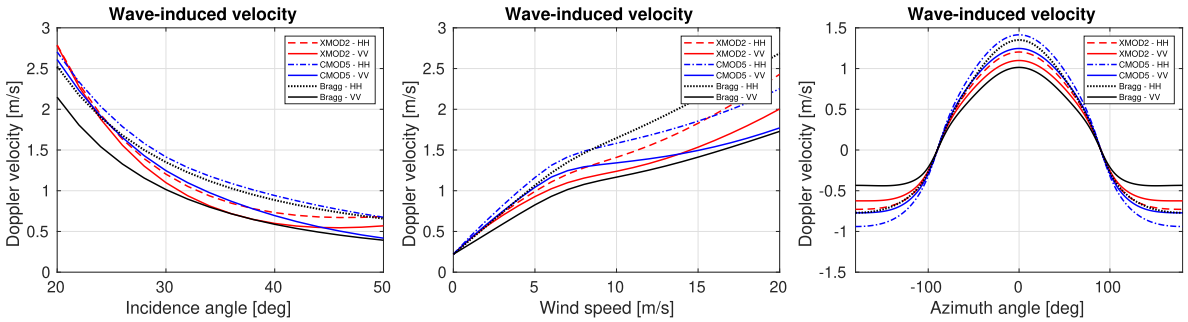

Fig. 4. Comparison of the wave-induced Doppler velocity simulated from tilt MTFs based on different NRCS models (see legend), long wave frequency $f = 0.15$ Hz, left: as a function of incidence angle ($U_{10} = 7$ m/s, $\varphi = 0°$), middle: as a function of wind speed ($\theta = 30°$, $\varphi = 0°$), right: as a function of wind direction ($U_{10} = 7$ m/s, $\theta = 30°$).

theoretical models due to the variety of possible parameterizations. This type of model is very dependent on the parameterization of the MTFs. This motivates the empirical approach, adopted in this work to estimate U_{wv}, discussed in Section IV-C. In the following, the Doppler model (5, called U_D model hereafter) is simulated using the empirical tilt MTF (derived from XMOD2 GMF) and the hydrodynamic MTF derived by Schmidt *et al.* [51]. The advantage of using empirical MTFs is they naturally include all scattering mechanisms.

III. Data Set

The objective of this study is to investigate the empirical relationship between the measured SAR dc and the sea surface wind vectors. The dc is estimated from the TanDEM-X data and the wind vectors are obtained from a reanalysis product. A detailed description of these two data sets is provided in Sections III-A and III-B.

A. Satellite Data

The satellite data were acquired by the TanDEM-X system [59]. TanDEM-X is a high-resolution interferometric SAR mission that consists of two satellites (TerraSAR-X and TanDEM-X) carrying identical X-band SAR sensors and flying in a close tandem formation [59]. The data set used in this study is called Coregistered Single look Slant range Complex (CoSSC) [34]. Part of this data set was acquired during an experimental short baseline measurement campaign. The TanDEM-X data used here were acquired in bistatic, stripmap, and single receive antenna mode. The scene size of each acquisition is about 50 km in azimuth and 30 km in range. This image size is specific to TerraSAR-X stripmap mode data and corresponds to one frame. The SAR can run for several frames in a row, making the imaged scene much longer than 50 km, such as the one in Fig. 8. The spatial resolution of raw (single look) images is $\sim$3.3 m and $\sim$2 m in azimuth and ground range, respectively.

For the study, data that were acquired over the ocean, with latitudes between $-75°$ and $+75°$ and satisfied the along-track baseline requirement were selected. Note that the coherence degrades with increasing along-track baseline because of the temporal decorrelation of the backscattered signal [60]. However, setting the baseline threshold too low (high coherence) for data selection would eliminate too many images. Based on the studies in [61] and [60], the baseline threshold was set to 100 m, which is a compromise between acceptable coherence and sufficient data size for the study. The southern hemisphere was excluded since very few acquisitions satisfy the imaging requirement. Both ascending and descending passes were used. Most of the images were acquired during August to September 2014 and October to November 2015 (plus a few acquisitions scattered in time between 2011 and 2016). Deriving the absolute geophysical dc (Doppler anomaly) from bistatic spaceborne InSAR system data such as TanDEM-X is challenging. Thus, we rely on acquisitions that contain land for phase calibration. Consequently, the proximity of the satellite scene to land is used as an additional criterion for data selection. Over 300 TanDEM-X image pairs were selected including single-polarized and dual-polarized acquisitions. The geographical locations of the selected acquisitions are shown in Fig. 5. Note that all the selected satellite scenes are acquired in coastal areas. It can be observed that the acquisitions are mainly located in the Baltic Sea, along the Norwegian coast, in the Mediterranean Sea, along the East/West US coast, and in the Sea of Okhotsk.

The NRCS is computed from each single look complex (SLC) SAR image and calibrated using the calibration factors provided in the CoSSC product. The absolute radiometric accuracy is 0.6 dB [62]. The interferometric phase is computed from each CoSSC pair. To further reduce the phase noise and thus improve the phase precision, multilooking, i.e., spatially averaging 50 by 50 pixels, is applied to the complex interferogram. This reduces the spatial resolution to $\sim$100 m. Given the hybrid (across and along-track interferometer) nature of TanDEM-X system, the phase is also sensitive to topography. Thus, the topographic phase is simulated, using a digital elevation model, and removed from the total phase. Phase calibration consists of the estimation of the bias of the residual phase over land and removal of this bias from the total phase (see [8] for details). The phase uncertainty is estimated, over land, to be about 0.06 radian [8]. In addition, the coherence is estimated from the CoSSC pair as an indicator of the phase quality. Finally, the phase is converted to Doppler shift and radial ground velocity using 1.

Fig. 6 shows (from left to right) the distribution of wind speed, wind direction, incidence angles, and temporal baseline

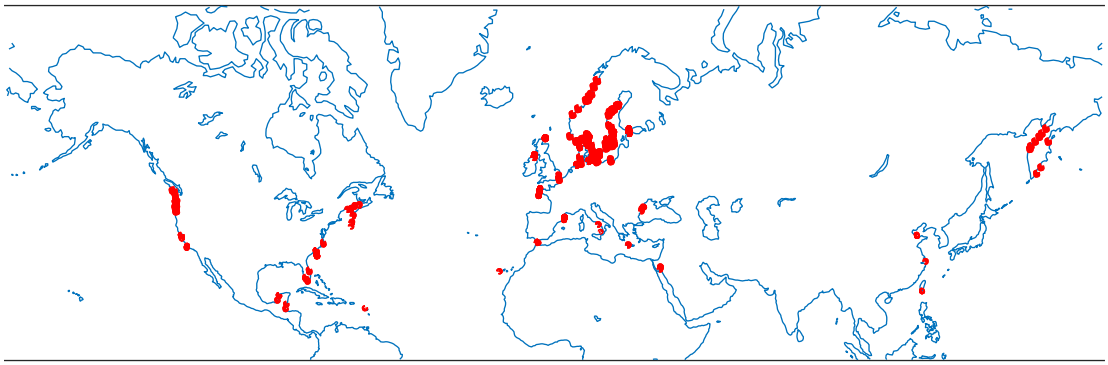

Fig. 5. Map of the locations of the TanDEM-X acquisitions used in this study.

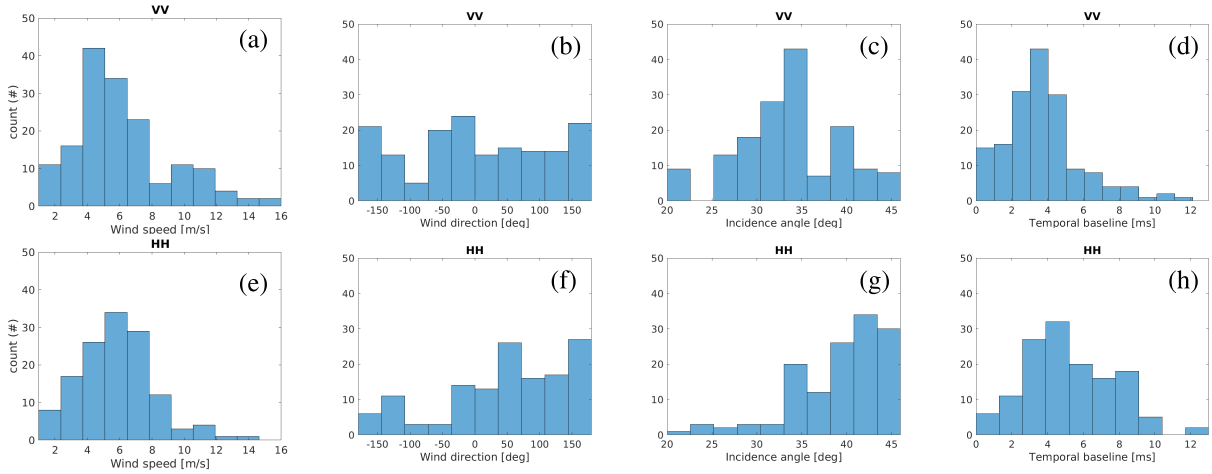

Fig. 6. Distribution of wind and acquisition parameters. (a) and (e) Wind speed U_{10}. (b) and (f) Wind direction (relative to LOS), according to ERA5. (c) and (g) Incidence angle. (d) and (h) Temporal baseline. (a)–(d) VV polarization. (e)–(h) HH polarization.

for VV acquisitions (top) and HH acquisitions (bottom). There are a few features to observe in these statistics, such as a dip in the relative wind direction distribution around $-90°$ in both VV and HH. It can be attributed to the fact that the data are acquired in the westerlies and trade wind zones and the satellite is in near-polar orbit looking to the right. Hence most of the acquisitions lie in the upwind (0) and downwind (± 180). The data in both polarizations cover roughly the same wind speed range with a peak around 4–6 m/s, though VV samples higher wind speeds. The incidence angles covered by the data in each polarization is however quite different, the histograms peak around 34° for the VV and 42° for the HH data. This hinders the comparison of the two polarizations using all the data. We found a few dual-polarized acquisitions which are used for comparison (see Section IV-E). Finally, temporal baselines span a relatively large range from 0.2 to 13 ms. The temporal baseline τ (also called InSAR time lag) is related to the spatial baseline B by the satellite velocity v as $\tau = B/v$. The highest temporal baseline ($\tau = 13$ ms) corresponds to the baseline threshold ($B = 100$ m) using TanDEM-X orbit velocity ($v = 7.68$ km/s). Note that the effective InSAR baseline is only half the physical baseline between the two antennas if only one of the antennas is used for transmitting and both for receiving, i.e., bistatic mode.

B. Wind and Wave Data

The wind and wave data are extracted from the hourly single layer (surface) ECMWF reanalysis (ERA) 5 reanalysis data set [63]. Though the quality of ERA5 product might not be optimal in coastal areas, it is the only product that provides hourly, global data set of an extensive list of atmosphere, land, and ocean variables from 1979 to present [63]. Note that the wind speed can also be retrieved from SAR NRCS [1]. The main atmospheric parameters used are the wind components (u_{10},v_{10}). The main oceanic parameters are the mean wave direction (mwd), mean direction of wind waves (mdww) and the Stokes drift components (u_S, v_S). The spatial resolution of the ERA5 data is 0.25° and 0.5° for the atmospheric and oceanic parameters, respectively, which is much coarser than that of SAR data ($\sim$100 m). As shown in Fig. 5, most of our data are acquired in coastal areas. Due to the coarse resolution of ERA5 compared to SAR, many acquisitions have no or sparse wave data.

The relationship between the wave direction and the wind direction is depicted in Fig. 7 for the mean direction of wind waves (bottom) and the mean wave direction (top). The latter includes wind-waves and swell. The data points shown in Fig. 7 correspond, in time and location, to the used satellite acquisitions. The wind-wave direction correlates very

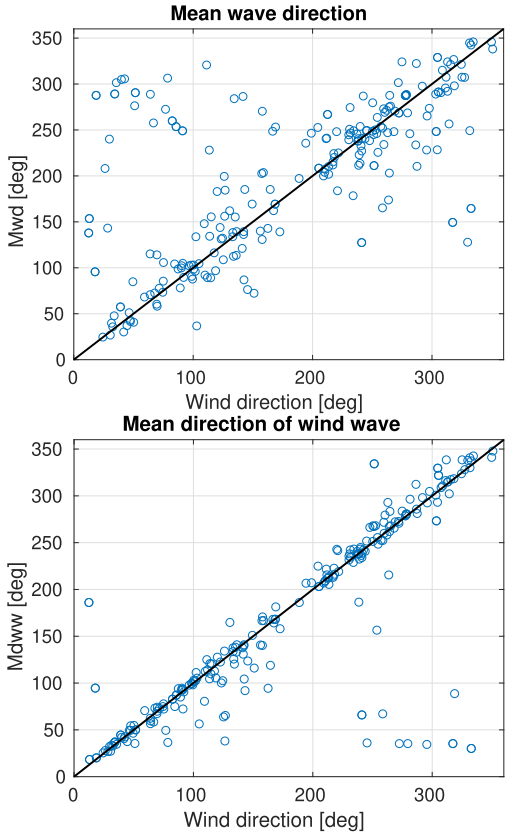

Fig. 7. Mean wave direction (top) and the mean wind wave direction (bottom) versus wind direction, from ERA5. Each data point corresponds in time and location to a TanDEM-X acquisition.

well with the wind direction except for a few anomalous cases, which justifies the use of wind direction as a proxy for wind-wave direction. The mean wave direction deviates in many cases from the wind direction, due to the presence of swell or refraction by topography. Ideally, an experiment matching SAR data to wave direction would require a global high resolution (<1–2 km) wave model which is not available now. Thus, given the good correlation between wind-wave and wind direction, we use the latter as a proxy to the former. We filter out the few cases where the wind and wind-wave direction differ by more than 90° when both are available. The swell larger than the pixel size (∼100 m) is resolved (by the image) and thus since the dc is averaged without power weighting over the whole image, this should cancel the swell modulation. There might be few residual cases where swell is unresolved, but we neglect this effect.

IV. Experimental Results

In the following plots, each data point is an average over a whole SAR image. As mentioned earlier, we rely on scenes that cover partially land for absolute calibration of the phase following the calibration method in [8]. We have selected 164 and 140 acquisitions in VV and HH polarization, respectively, for the study. This is a small data set compared to the amount of data generally used to build an empirical model, e.g., [7]. Therefore, we cannot afford binning the data in the three parameters incidence angle, wind speed, and direction. We only bin the data in a single parameter. Thus, the results are presented either as a function of incidence angle, wind speed, or wind direction.

In all our plots the convention is that the Doppler frequency/velocity is positive for approaching scatterers and negative for receding scatterers. The relative azimuth angle is 0 for upwind, ±90 for crosswind, and ±180 for downwind. The dc and U_D, in the plots, refer to the measured geophysical dc and radial horizontal velocity, respectively. In principle, now the estimated U_D represents the sum of U_{wv}, U_E and U_S.

To correct for the current contribution to Doppler velocity, a high-resolution ocean circulation model would be required, which is not available to us. To our knowledge, there is no publicly available ocean surface current product with the resolution (<1–2 km), the sampling (1–4 h), the coverage (northern hemisphere), and time extent (2011–2016) required for our analysis. Note that the characteristic spatial and temporal scale of coastal currents are small, compared to open ocean, being about 5–7 km and few hours to 1 day, respectively. For instance, to sample a semi-diurnal tidal current, at least a 6-hourly product is required. Thus, the correction for current is left for future work.

A. Example of Wind Dependence of the NRCS and DC

Fig. 8(a)–(d) depicts an example illustrating the spatial correlation between the wind variation (a), dc (b) and NRCS (c). Each image is a mosaic of four frames. It can be observed that the NRCS and dc signatures are dominated by the large-scale variation of the wind speed and direction. The high NRCS / positive dc in the upper part and the low NRCS / negative dc in the lower part of the image are clearly visible. Note that this is a descending pass with the antenna looking to the right, hence upwind in the upper part and cross-to-downwind in the lower part. The fourth frame (from top to bottom) of the NRCS image is shown (zoomed) in panel (d). The wind streaks suggest that the ERA5 wind vectors in the lower part of the wind image should be turning more to the left. Moreover, the NRCS values suggest a higher wind speed than the 1–2 m/s provided by ERA5. Using XMOD2, at this wind speed and incidence angle gives −24 dB which is lower than the measured values. This explains the relatively large negative dc in the fourth frame. Finally, the dc image contains, in addition to low order wind signature, higher-order modulations probably due to currents, river plumes, and bathymetric modulation.

B. NRCS Assessment

The tilt MTF used in the Doppler model above (see Fig. 1) is derived from the XMOD2 GMF which is built from data similar to the data used here (TanDEM-X). To assess the dependence on incidence angle, the calibrated sea backscatter is compared to the simulated NRCS from XMOD2 [46]. To convert from VV to HH, we used the PR model proposed in [58]. The lower limit of the wind speed is set to 2 m/s and the incidence angle range extends from 20° to 50°, but there are very few data points above 45°.

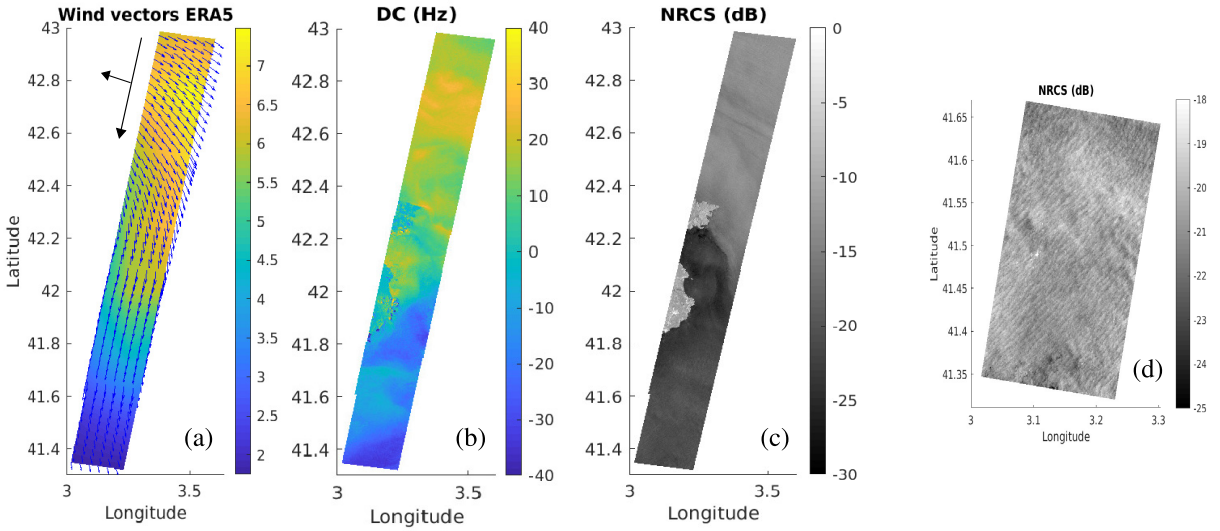

Fig. 8. Example of the dependence of dc and NRCS on wind speed and direction. (a) ERA5 wind vectors (colormap is wind speed in m/s). (b) DC in Hz. (c) NRCS in dB. (d) Blow-up of the southernmost frame of the image with optimized gray scaling, descending pass, right looking antenna, VV polarization, $\theta = 41.5°$. Acquisition time is 2014-08-19 05:54:11. The long and short arrows in panel (a) indicate the flight and the look directions, respectively.

The results are depicted in Figs. 9 and 10, for VV (upper panel) and HH (lower panel) polarizations. The NRCS data are binned by incidence angle (Fig. 9) and by wind speed (Fig. 10), including all wind directions. The size of the data points increases with wind speed from 2 m/s to 15 m/s (Fig. 9) and with incidence angle from 20° to 50° (Fig. 10). The wind direction is indicated by the color of the data points, i.e., red dots indicate upwind and blue dots indicate downwind. The size of the data points clearly correlates with the NRCS, i.e., it increases and decreases with NRCS values, in Figs. 9 and 10, respectively. The coloring, however, does not show an obvious clustering as a function of wind direction. This is due to the fact that the dependence of NRCS on wind direction is much weaker than its dependence on incidence angle and wind speed.

For the NRCS simulation using XMOD2 GMF, the mean wind speed is used as input for Fig. 9 and the mean incidence angle as input for Fig. 10. Both upwind and crosswind curves are plotted. Note that the upwind and crosswind give the maximum and minimum NRCS values for a given wind speed and incidence angle. In terms of the dependence of the NRCS on incidence angle, there is a good agreement between the data and XMOD2 up to 45°, i.e., the limit of validity range of XMOD2 [46]. There is however a slight systematic overestimation of XMOD2 values by about 1–2 dB. But note that the absolute value is not important for MTF calculations but rather the relative variations. The agreement is slightly worse at high incidence angles, i.e., close to the limit of validity of XMOD2. At these high incidence angles, the signal to noise ratio (SNR) is low hence the high uncertainty in the measurements. Overall, the variation with incidence angle and wind speed is well reproduced by the GMF, which is most relevant for the MTF calculation.

C. Doppler Velocity Assessment

The coherence threshold is set to 0.2 during the averaging within the image. That is only pixels with coherence higher than the threshold are averaged. In addition to the degradation of coherence with the increasing baseline mentioned above, the coherence decreases with decreasing SNR. Since the SNR decreases with incidence angle and it decreases more rapidly for HH than for VV. The coherence threshold is set relatively low in order to include measurements at high incidence angles for both HH and VV.

The underlying assumption of the empirical approach is that if a number of measurements corresponding to the same wind vector are averaged, the variability due to currents (uncorrelated with the local wind) should vanish. This is achieved by combining data from ascending and descending passes, acquisitions in different areas and different times, i.e., sampling different current magnitudes and directions. Note that the current characteristic (spatial) scale, in coastal areas, is relatively small (5–10 km) compared to the image size (50 km). Similarly, random phase errors (due to SAR system, processing, and ERA5 wind) should vanish after averaging, while a possible systematic bias would shift and scale all dc points by the same amount.

To avoid strongly biased dc, images acquired over known persistent and strong currents, e.g., the Norwegian coastal current and the tidal current in the Orkney Islands, are removed. After coherence thresholding and filtering images with strong currents, 134 and 119 acquisitions for VV and HH polarization, respectively, were selected for Doppler analysis.

1) Doppler Variation With Incidence Angle: According to the model described in Section II, it is expected that the wave-induced Doppler velocity should decrease with increasing incidence angle. This is mainly due to the tilt MTF decreasing with incidence angle (see Fig. 1). The estimated U_D is depicted in Fig. 11 as a function of incidence angle for VV (top) and HH (bottom) polarization, including all wind speeds and directions. The size of the data points increases with wind speed and the color indicates the relative wind direction. The coloring clearly separates the data points into two clusters,

TABLE I

AVERAGE PARAMETERS FOR DOPPLER VELOCITY SIMULATIONS IN FIGS. 11–14. THE MEAN INCIDENCE ANGLE $\langle\theta\rangle$ IS CALCULATED FROM THE DATA. THE WIND SPEED $\langle U_{10}\rangle$, SIGNIFICANT WAVE HEIGHT $\langle H_s\rangle$, PEAK FREQUENCY $\langle\omega_p\rangle$ AND STOKES DRIFT $\langle U_s\rangle$ ARE OBTAINED FROM ERA5. THE VALUES IN PARENTHESES REFER TO UPWIND-DOWNWIND

Parameter Unit	$\langle\theta\rangle$ [deg]	$\langle U_{10}\rangle$ [m/s]	$\langle H_s\rangle$ [m]	$\langle\omega_p\rangle$ [rad/s]	$\langle U_s\rangle$ [m/s]
VV	33.72 (34.7-33.00)	5.52 (6.63-6.028)	1.094 (1.052-0.89)	0.97 (1.11-1.078)	0.074 (0.083-0.064)
HH	40.56 (37.81-39.82)	5.83 (5.73-6.53)	1.057 (0.88-1.19)	1.00 (1.08-0.94)	0.073 (0.060-0.083)

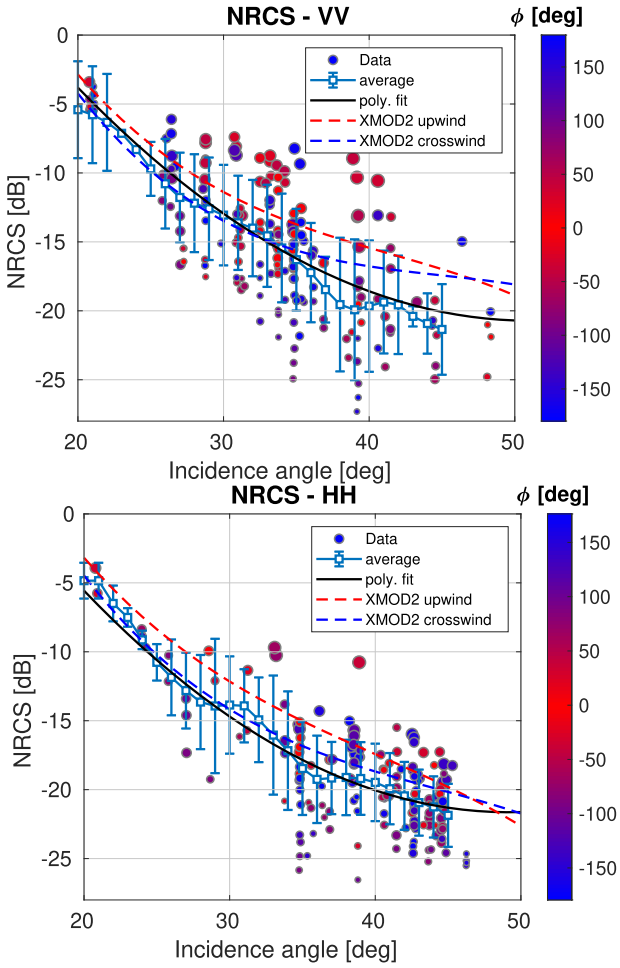

Fig. 9. NRCS dependence on incidence angle for VV (top) and HH (bottom) polarization. Solid lines are the polynomial fit (black) and average (blue) with error bars ($\pm\sigma_{U_D}$). Dashed line is XMOD2 simulated with mean wind speed (5.47 m/s for VV and 5.88 m/s for HH). The size of the data points increases with wind speed from 2 m/s to 15 m/s and the color indicates the relative wind direction (see colorbar).

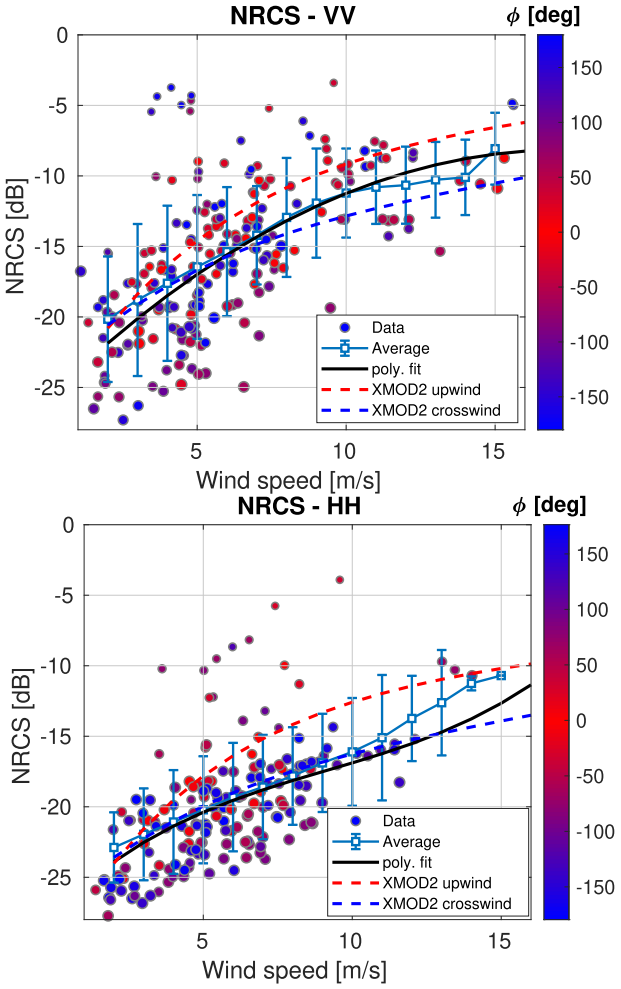

Fig. 10. NRCS dependence on ERA5 wind speed for VV (top) and HH (bottom) polarization. Solid lines are the polynomial fit (black) and average (blue) with error bars ($\pm\sigma_{U_D}$). Dashed line is XMOD2 simulated with mean incidence angle (33.7° for VV and 40° for HH). The size of data points increases with incidence angle from 20° to 50° and the color indicates the relative wind direction (see colorbar).

upwind (red, positive) and downwind (blue, negative) for both polarizations. The clustering due to wind speed variation is however not clear. This is due to the fact that the U_D dependence on wind speed is weaker than its dependence on incidence angle (see Fig. 4). The scatter of the data points is also due to surface current contribution and to possible phase calibration and ERA5 wind errors. For comparison, the U_D model (5) with the wave parameters given in Table I, the C-band Doppler (CDOP) and KaDOP models are also plotted as dashed, dash-dotted and dotted curves, respectively. The shaded area represents the wind-induced drift current (3% of U_{10}).

Despite the scatter and the relatively small data set the average curve, for the VV polarization, shows a clear decrease of U_D in magnitude, with increasing incidence angle. The general trend, i.e., $|U_D|$ decrease with increasing θ, is qualitatively consistent with the three models and also in agreement with previous studies [17], [54]. Note that the trend is stronger and more consistent with the U_D models in the downwind direction than in the upwind direction. For the HH polarization, the trend is much less clear, but according to our data, there is a slight decrease up to 35° and an increase at higher incidence angles.

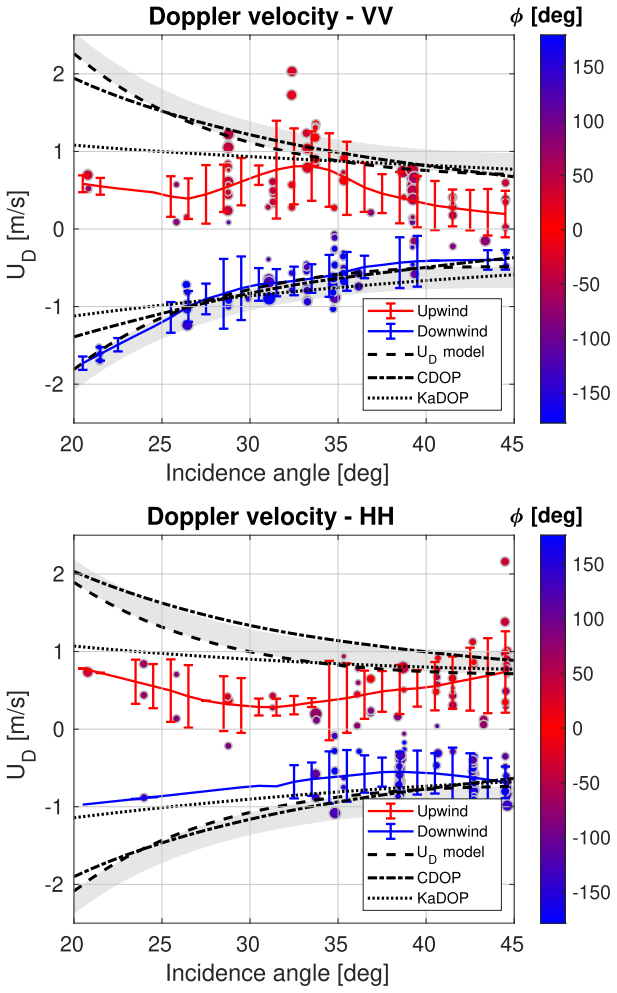

Fig. 11. Estimated U_D as a function of incidence angle for VV (top) and HH (bottom), all wind speeds and directions included. The size of the data points increases with wind speed from 2 m/s to 15 m/s and the color indicates the relative wind direction (see colorbar). The solid curves represent the average with error bars ($\pm\sigma_{U_D}$). See legend for the other curves.

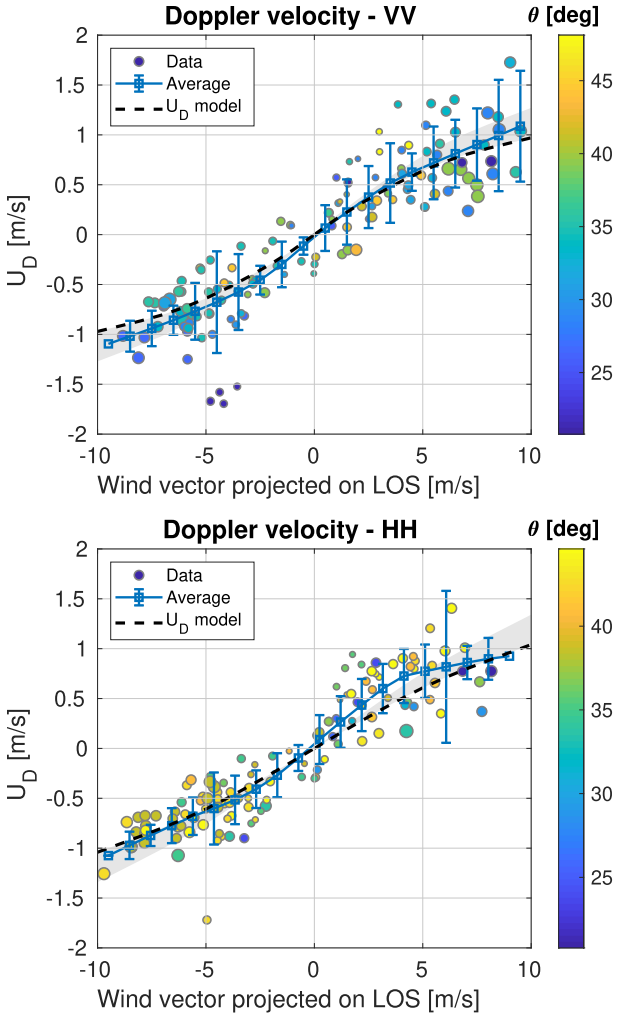

Fig. 12. Estimated U_D as a function of the radial wind, for VV (top) and HH (bottom) polarization, all incidence angles included. The size of the data points increases with wind speed from 2 m/s to 15 m/s and the color indicates incidence angle (see colorbar). The solid curve represents the average with error bars ($\pm\sigma_{U_D}$) and the dashed curve represents the U_D model (5).

This behavior is in disagreement with the U_D models which predict a decrease for both polarizations and wind directions.

The three models are more consistent with the data around the mean incidence angle ($\sim$34° for VV and $\sim$40° for HH). At lower incidence angles ($\lesssim$30°), the models and data deviate significantly. Also, the upwind values are lower than downwind values, in this region, which contradicts the theory and previously reported results. Note however that the data is sparse in that region, e.g., only one point in HH. Moreover, the wind speeds in the upwind and downwind are slightly different (see Table I). Therefore, our result should not be considered as reliable in the region $\theta \lesssim 30°$, and thus the derived empirical U_D model (suggested later) is only valid around the mean incidence angle.

Finally, note that the decrease rate, of $|U_D|$ vs θ, given by KaDOP is systematically lower than both our model and CDOP. This might be due to the large difference in frequency and/or processing techniques. The KaDOP model is based on a sea platform real aperture radar operating at Ka-band, while our study and CDOP are based on satellite SAR. This disagreement deserves further investigation which is left for future work.

2) Doppler Variation With Radial Wind Speed: The variation of dc with the wind speed is illustrated in Fig. 12, which depicts the estimated Doppler velocity U_D as a function of the radial wind U_{10r}, including all incidence angles. U_{10r} is calculated as the dot product between the wind vector $\vec{U}_{10}$ and the radar look vector $\vec{l}$ (determined by the satellite heading and the nominal antenna look angle relative to azimuth, 90°). The size of the data points increases with wind speed and the color indicates incidence angle. Few outliers can be identified with lowest (highest $|U_D|$) and highest (highest $|U_D|$) incidence angles for VV and HH, respectively. The U_D model based on 5, with the parameters given in Table I, is also plotted (dashed curve) for comparison. The shaded area represents the wind-induced drift current.

Despite the scatter, the correlation between U_D and radial wind speed is evident. The variation of U_D as a function U_{10r} is quasilinear in the range of -5 to $+5$ m/s and becomes

slightly nonlinear at higher radial wind speeds. The average curves (solid blue) are very similar to Fig. 5 in [5], Fig. 2 in [16] and Fig. 5 in [19]. The U_D model is also very close to the average curve. The scatter (deviation from the mean curve) is due to including all incidence angles, current contribution and possible phase calibration, and ERA5 wind errors.

To summarize, the figure indicates that $|U_D|$ increases with increasing radial wind speed, i.e., $|U_D|$ is maximum when the wind is strong and parallel to the radar range direction and is minimum (close to zero) when the wind is weak and perpendicular to the range direction. This is in qualitative agreement with the conclusions in [5], [16], and [19]. Quantitatively, U_D amounts to about 15% of the radial wind speed for VV polarization, which is consistent with [5], considering the difference in incidence angle between our data (33°) and the data used in [5] (23°). For HH, U_D also amounts to about 15% of the radial wind speed but at a higher incidence angle (40°), which indicates that U_D is larger at HH than at VV polarization.

3) Doppler Variation With Relative Wind Direction: The variation of dc with wind direction is illustrated in Fig. 13, which depicts the Doppler velocity U_D as a function of the relative wind direction, i.e., the difference between the radar look direction and wind direction. All incidence angles and wind speeds are included. The size of the data points increases with wind speed and the color indicates incidence angle. Similar to Fig. 12, few outliers can be identified with the lowest and highest incidence angles for VV and HH, respectively. The U_D model (5) simulated using the parameters given in Table I is also plotted (dashed curve) for comparison. The scatter around the mean curve is also due to current contribution and to phase and wind errors.

Despite the scatter of the data points, Fig. 13 shows that the average curve (blue) and the fit curve (red) follow the anticipated (see Figs. 3 and 4, right panel) sinusoidal-like variation, i.e., the U_D has its maximum and (negative) minimum values in the upwind and downwind directions, respectively, and vanishes close to the crosswind direction. These curves also exhibit a slight upwind/downwind asymmetry but this should be taken with caution since the mean incidence angle and wind speed are not exactly the same between the upwind and the downwind data. The U_D model (taking into account the current drift) reproduces well the variation except for a slight underestimation in the downwind direction. Our result compares also qualitatively well, in terms of U_D variation with relative wind direction, with [18, Fig. 26]. Though at a different frequency and incidence angle, the latter study shows a similar sinusoidal variation of U_D with absolute values in the upwind/downwind between 0.5 and 1 m/s and close to zero in the crosswind direction.

A truncated (at the second order) Fourier series as a function of azimuth direction is chosen as a model to fit the data

$$U_D(\phi) = B_0 + B_1 \cos(\phi) + B_2 \cos(2\phi) \tag{6}$$

where ϕ is the relative wind direction. The B coefficients should usually vary with incidence angle and wind speed. Due to the limited amount of data, the coefficients are only fit at the mean incidence angle and wind speed, thus they are constants

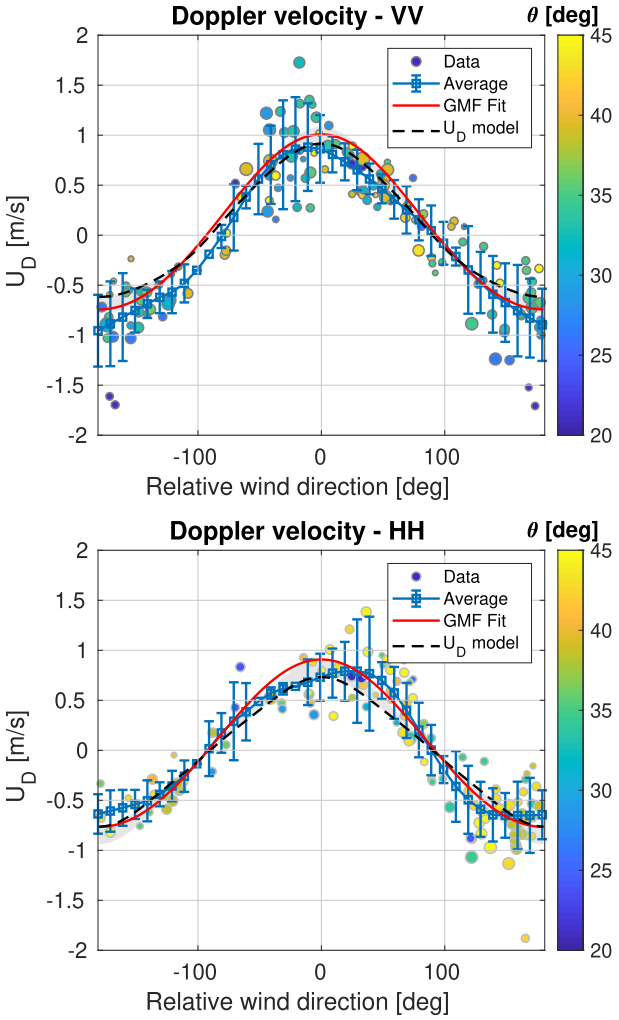

Fig. 13. Estimated U_D as a function of relative wind direction, for VV (top) and HH (bottom) polarization, all incidence angles and wind speeds included. The size of the data points increases with wind speed from 2 m/s to 15 m/s and the color indicates incidence angle (see colorbar). The blue curve represents the average with error bars ($\pm\sigma_{U_D}$), the red curve is the GMF fit (6) and the dashed curve is the U_D model (5).

here. The obtained coefficients are given in Table II for both polarizations. This should not be used as a general model, since it is only valid for a given distribution of incidence angles and wind speeds. Inspection of Figs. 11 and 13 suggests that the U_D GMF (6) is valid in the incidence angle range ∼30–40° and ∼35–45° for VV and HH, respectively, and more reliable around the mean incidence angles. Outside this region, unexplained results are obtained, e.g., downwind larger than upwind (see Fig. 11). The data density around the crosswind direction (±90°) is quite low, reducing the confidence in the B coefficients. However, the suggested GMF agrees well with other studies (see comparison below). Note also that B_1 in HH polarization (despite the higher incidence angles in HH) is close to the value found for VV polarization. The PD is investigated in more detail in Section IV-E.

D. Comparison With Other Models and Data Sets

In this section, the empirical GMF (6) fit to data-estimated U_D, as a function of relative wind direction, is compared to other models and data sets. The models and data sets used for

TABLE II
B COEFFICIENTS

Polarization	B_0	B_1	B_2
VV	0.0914	0.8738	0.0539
HH	0.0443	0.8558	0.0281

comparison are the following: I) the numerical MTF-based model (M4S) developed in [15] based on an improved composite surface model and an improved Apel's wave spectrum parameterization [21], validity: L to Ka bands, VV, and HH polarization, 2 m/s $\leq U_{10} \leq$ 20 m/s. II) the empirical model called CDOP built from global ENVISAT/ASAR data [7], validity: C-band SAR, VV and HH, 17° $\leq \theta \leq$ 42°, 1 m/s $\leq U_{10} \leq$ 17 m/s. III) the Wavemill Proof-of-Concept airborne campaign data set [54], validity: X-band, VV, 27° $\leq \theta \leq$ 43°, $U_{10} = 5.5$ m/s. IV) the semi-empirical model KaDOP built from data acquired by a sea platform-borne scatterometer in the Black Sea [19], validity: Ka-band, VV and HH, 0° $\leq \theta \leq$ 65°, 3 m/s $\leq U_{10} \leq$ 15 m/s. In addition, our U_D model (5) is also plotted for comparison. All the compared data sets and models are converted to surface Doppler velocity. Our U_D model and the Wavemill data set are provided in terms of surface velocity in m/s. The M4S and CDOP models provide the dc in Hz, they are converted by $U_D = cf_D/(2f_e \sin\langle\theta\rangle)$, where f_D is the model-simulated dc, c is the speed of light and f_e is the radar frequency which equals 9.650 GHz and 5.331 GHz for M4S and CDOP, respectively. The KaDOP calculates the radial Doppler velocity, thus it is converted as $U_D = U_{\rm DC}/\sin\langle\theta\rangle$, where $U_{\rm DC}$ is the quantity provided by the model. All the models and GMFs were fed with the mean incidence angle $\langle\theta\rangle$ and mean wind speed $\langle U_{10}\rangle$ (given in Table I). In addition, KaDOP was fed with the significant wave height $\langle H_s\rangle$ and the peak wave frequency $\langle\omega_p\rangle$ (given in Table I), without swell and drift current.

As mentioned earlier, the estimated U_D contains wave-induced velocity, the surface Ekman current, and the Stokes drift. The latter two components are often parameterized in wind speed

$$U_D = U_{\rm wv} + (U_E + U_S)\cos\phi \quad (7)$$
$$= U_{\rm wv} + (\alpha_1 + \alpha_2)U_{10}\cos\phi. \quad (8)$$

In a rigorous parameterization, α_1 should have a regional and seasonal dependence due to ocean stratification [56], [64]. The factor α_2 should also depend on the fetch [55] and the sea state [56]. In practice, α_1 and α_2 are often taken as constants. The sum of the two factors $(\alpha_1 + \alpha_2)$ is estimated to be ≈0.03 [55], [56].

The comparison of different models and data sets is a delicate task because each model/data set represents different sea states (wave spectrum). In addition, they contain different contributions of U_E and U_S depending on the data processing. The MTF-based models represents $U_{\rm wv}$ only (without U_E and U_S). For the CDOP model [7], the authors state that strong currents have been filtered out. In the Wavemill data, a measured acoustic Doppler current profiler (ADCP) current was removed from the measured U_D [54]. In KaDOP data, the dc was corrected for the surface current measured at 10 m depth. Usually, when models of $U_{\rm wv}$ are compared to other data sets a drift current (3% of U_{10}) is added to these models, e.g., [17], [19]. Here, we have not subtracted (nor added) any quantity from our data. Thus our GMF should represent an estimate of the total observed U_D. For the comparison, a portion of the wind speed with a factor ranging from 0 to $\alpha_1 + \alpha_2$ is added as a shaded area to the U_D model, where $\alpha_1 = \overline{U}_S/\overline{U}_{10}$ and $\alpha_2 = 0.015$. $\overline{U}_S$ and $\overline{U}_{10}$ are the ERA5 average (over the whole data set) Stokes drift and wind speed, respectively. The shaded area is shown to remind the reader to take into account the natural difference between the MTF-based models that simulate $U_{\rm wv}$ and the empirical models that potentially include the wind-induced drift current in addition to $U_{\rm wv}$.

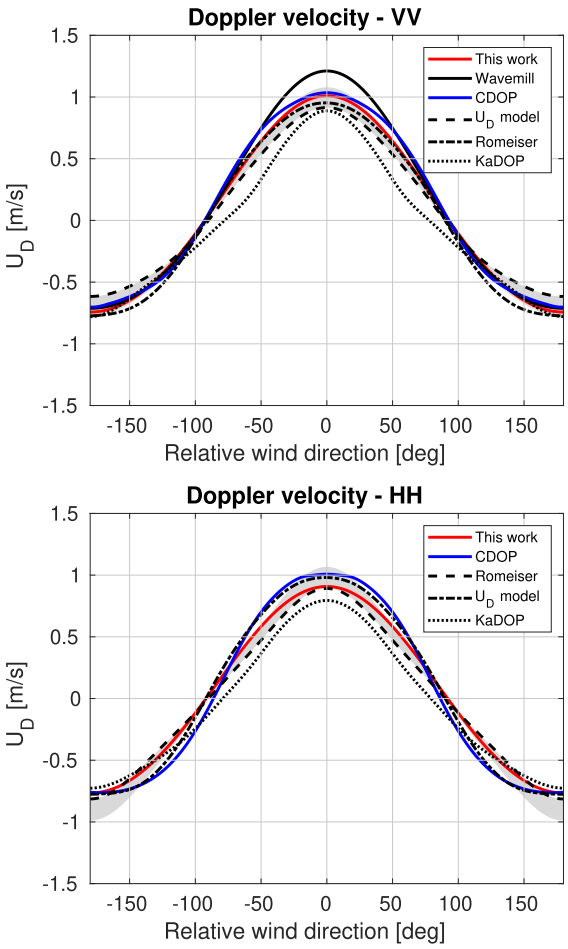

Fig. 14. Comparison against other data sets and models as a function of relative wind direction, for VV (top) and HH (bottom) polarizations. The solid red curve is the U_D GMF (6) and the dashed black curve is the U_D model (5). For the other curves see legend. The shaded area is equal to $(\alpha_1+\alpha_2)U_{10}$ (see text for details).

Fig. 14 shows the comparison of our GMF against the above-mentioned models for VV (top) and HH (bottom) polarization. The shaded area is the interval $[0, (\alpha_1+\alpha_2)U_{10}]$ added to the U_D model (dashed line). Generally, the different models are roughly in good agreement within 0.2 m/s (taking into account the wind-induced drift current when comparing the MTF-based models against measured U_D). The main

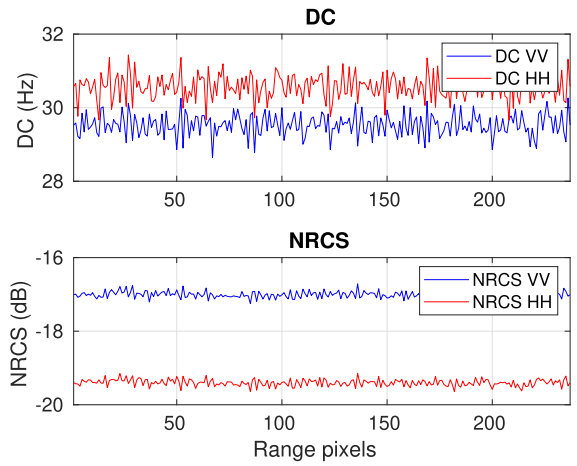

Fig. 15. Comparison of VV and HH, dc (top) and NRCS (bottom), range profiles, $\theta = 35°$, $U_{10} = 6$ m/s.

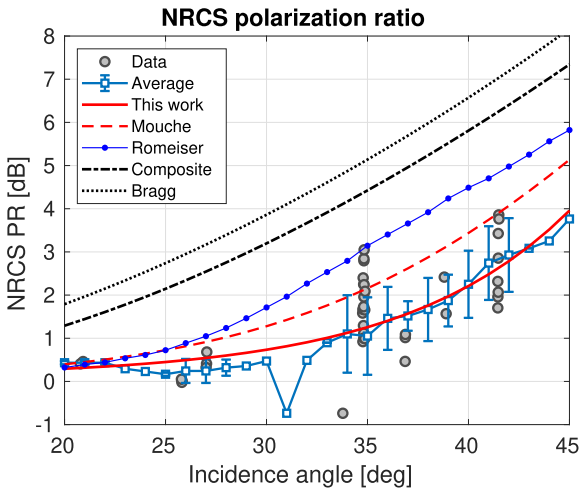

Fig. 16. Polarization ratio (PR $= \sigma^0_{VV}/\sigma^0_{HH}$). Measured PR (circles) and average curve with error bars (solid cyan), empirical fit to the data (solid red), empirical model from [57] (dashed red), numerical model from [21] (solid blue with dots), composite surface model (dashed black), pure Bragg model (dotted black).

noticeable differences between models are in the upwind and downwind directions, with the difference in the upwind being larger than in the downwind. In the downwind direction all models give very close values except our U_D model which deviates slightly for VV polarization. KaDOP shows, unlike other models, a slightly narrower distribution and negative U_D in the crosswind direction, which was previously noted and discussed in [19]. For VV polarization and upwind, our GMF is very close to CDOP while it gives a value that is approximately 0.2 m/s smaller than Wavemill. This is in agreement with [19] [see their Fig. 9(a)], i.e., Wavemill gives the largest upwind dc followed by CDOP and KaDOP. For HH polarization, our GMF gives a value that is ∼0.1 m/s smaller than CDOP in the upwind direction, while they almost match in the downwind direction.

E. PR and PD

In this section, we will analyze the properties of our dual-polarized data set. Fig. 15 depicts an example of the range profile (averaged over azimuth) of the NRCS and dc for VV and HH at $\theta = 35°$. It can be observed that $\mathrm{dc_{HH}}$ is larger than $\mathrm{dc_{VV}}$ and σ^0_{VV} is larger than σ^0_{HH}. This is qualitatively in agreement with the simulation results from our Doppler model (Fig. 3). The difference between $\mathrm{NRCS_{VV}}$ and $\mathrm{NRCS_{HH}}$ is about 2.5 dB. The PR and PD are investigated quantitatively below, using all the dual-polarized data over the sea, and compared to theoretical and empirical models.

1) Polarization Ratio: The measured NRCS PR defined as PR $= \sigma^0_{VV}/\sigma^0_{HH}$ is depicted in Fig. 16. The figure shows that the PR is systematically larger than 1 (0 dB), indicating that in all cases except one, σ^0_{VV} is larger than σ^0_{HH}. The figure also shows that the measured PR is significantly lower than the PR predicted by the Bragg theory in both forms, the pure Bragg and composite surface models, by 2 to 3 dB. Although this data set is small, there is a clear increase of PR with incidence angle. An empirical model of the form $\mathrm{PR}(\theta) = A\exp(B\theta) + C$ is fit to the data (in dB) and the obtained coefficients are: $A = 0.0167$, $B = 0.1209$, $C = 0.1063$. The empirical fit is depicted by the solid red curve. For comparison, we have also plotted the empirical PR model from [57] and the PR calculated using the numerical model from [21]. All the theoretical models overestimate the PR and its increase rate with incidence angle. The empirical PR model by [57] also slightly overestimates the PR but is the closest to our empirical fit followed by the numerical model [21].

The discrepancy between measured PR and the theoretical Bragg PR is often used as an indicator of non-Bragg (non-polarized) scattering associated with radar returns from wave breaking and specular reflections from the regular surface at low incidence [22], [43], [65]–[67]. According to [66] and [67], the measured PR and Bragg composite PR can be used to estimate the non-Bragg scattering contribution. Using (11) in [67], the composite model PR and the measured PR values shown in Fig. 16, the ratio of non-Bragg to Bragg NRCS varies between 0.4 and 2.6 for VV, and between 1.9 and 4.5 for HH. Around the mean incidence angles (∼34 for VV and ∼40 for HH), the non-Bragg contribution to the NRCS exceeds the Bragg contribution by a factor ∼2 and ∼3 for VV and HH, respectively.

2) Polarization Difference: The dc PD defined as PD $= |\mathrm{dc_{VV}}| - |\mathrm{dc_{HH}}|$, is depicted in Fig. 17. The figure shows that the PD is systematically lower than 0 Hz, indicating that $\mathrm{dc_{HH}}$ is higher than $\mathrm{dc_{VV}}$. Also, the measured PD is significantly lower, in absolute value, than the PD predicted by the Bragg theory (pure Bragg and composite surface models). Despite the small size of the data set, there is a clear increase, in the absolute value, of PD with incidence angle. We have calculated the PD using our Doppler model with the tilt MTF from NRCS data, XMOD2, CMOD5, composite surface model, pure Bragg, and the PD calculated using the M4S model [15]. All theoretical models overestimate, in absolute value, the PD. The PD calculated using our Doppler model with the tilt MTFs derived from the NRCS data and XMOD2 are the most consistent with the measured PD, followed by the CMOD5 and

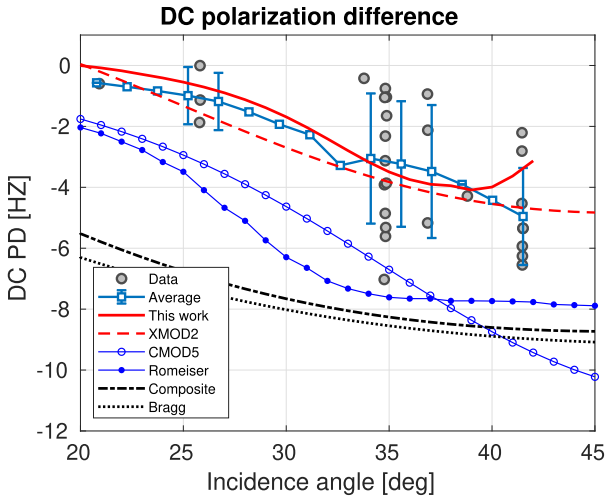

Fig. 17. DC polarization difference (PD $= |\mathrm{dc_{VV}}| - |\mathrm{dc_{HH}}|$). Measured dc (circles) and average curve with error bars (solid cyan). PD using tilt MTF calculated from, dual-pol NRCS data (solid red), XMOD2 (dashed red), CMOD5 (solid blue with circles), composite surface model (dashed black), pure Bragg model (dotted black), PD from M4S model [15] (solid blue with dots).

the M4S model [15]. The Bragg models overestimate the PD by ∼4 to 6 Hz.

V. Discussion and Conclusion

First, we have compared the tilt MTF simulated with different NRCS models and also compared different hydrodynamic MTF models. We have shown that using different MTF parameterizations affects the simulation of the wave-induced Doppler velocity (U_{wv}), in the absolute value (by up to 0.5 m/s) and also in its variation with incidence angle, wind speed, and direction; and the difference between polarizations.

Second, the comparison of the measured NRCS against the XMOD2 GMF showed that the incidence angle and wind speed dependences are relatively well reproduced by the GMF at both polarizations VV and HH, though the absolute value is overestimated by $\sim 1-2$ dB. This suggests that the tilt MTF can be derived directly from the empirical GMF. Thus, we suggested a semi-empirical Doppler model based on empirical tilt and hydrodynamic MTFs.

Third, the general characteristics of the dc derived from the X-band ATI phase and converted to horizontal velocity (U_D) were analyzed. It was found that U_D decreases in absolute value with incidence angle for VV polarization which is in agreement with our simulations and previous studies (CDOP, Wavemill, and KaDOP). For HH polarization, U_D decreases with incidence angle up to ∼35° and then increases which is in disagreement with the models. The decrease rate of KaDOP [19] is systematically smaller than both our U_D model and CDOP for both polarizations. This disagreement in the behavior of U_D as a function of incidence angle deserves further investigation, which is left for future work.

Our analysis also showed that U_D increases, in magnitude, quasi-linearly with the radial wind (wind vector projected on the LOS) in the range of [–5,5] m/s and becomes slightly nonlinear at radial wind speeds higher than ∼5 m/s, which agrees with [5], [16]. The contribution of the wind to U_D corresponds to about 15% of the radial wind speed. This value is consistent (taking into account the difference in incidence angle) with the 30% reported by [5] at C-band, VV, and $\theta = 23°$. Finally, the estimated U_D varies sinusoidally with relative wind direction, it has maxima at upwind and downwind and vanishes at crosswind with slight upwind/downwind asymmetry. This U_D variation is in agreement with our theoretical simulations (see Fig. 3). This is also in qualitative agreement with the Ka-band study in [18] (see their Fig. 26). The U_D values reported in the latter study are lower, due to the higher incidence angle (56°), but they still lie in the range [0.5, 1] m/s and $[-1, -0.5]$ for the upwind and downwind, respectively. This suggests that the incidence angle dependence is probably stronger than the radar frequency dependence.

Fourth, we fit an empirical GMF to our data and compared the empirical fit (6) with the coefficients given in Table II to: 1) the numerical model (M4S) [15] 2) the C-band empirical model (CDOP) [7] 3) experimental results published by the Wavemill team [54] and 4) the Ka-band semi-empirical model (KaDOP) [19]. In addition, our U_D model (5) presented in Section II, was also plotted for comparison. Note that the MTF-based models (M4S, KaDOP and our U_D model) simulate only the wave-induced contribution (U_{wv}), while the empirical GMFs (CDOP, Wavemill and our GMF) contain, in principle, also the wind-induced drift current, i.e., $(U_{\mathrm{wv}} + U_E + U_S)$. The main difficulty in comparing MTF-based models to empirical models/data sets resides in the estimation of the $(U_E + U_S)$ contribution.

Nevertheless, our GMF compares generally well with the four models, with all differences within ∼0.2 m/s. More specifically, in the downwind direction and for both polarizations, all the models give very close values except our U_D model which slightly underestimates U_D for VV. In the upwind direction and for VV, our GMF is very close to CDOP but is ∼0.2 m/s lower than Wavemill. The difference between CDOP and Wavemill has already been noticed and discussed in [54]. For HH polarization, our GMF is slightly lower than CDOP by about ∼0.1 m/s. We should mention that the incidence angles in the downwind are closer to the mean incidence angle $\langle\theta\rangle$ than in the upwind (see Table I). Since all models are fed with $\langle\theta\rangle$, this might explain the slightly better match at downwind than upwind. Moreover, it is well known [22], [65], [68] that the non-Bragg scattering by breaking waves is stronger (maximum) in the upwind direction. This might also explain the slightly better agreement between models and data sets at downwind than upwind. The deviation of the MTF-based models from CDOP and our GMF can, to some extent, be explained by the drift current in both upwind and downwind while the difference between MTF-based models and the Wavemill exceeds the drift current in the upwind. Finally, though KaDOP gives in general slightly lower U_D values, it is difficult to draw a conclusion about the radar frequency dependence. For instance, the difference between CDOP and Wavemill is larger than the difference between CDOP and KaDOP.

The differences between the compared models might be explained by different sea states, i.e., wave spectra. The presence of swell, for instance, affects U_D as discussed in [19].

Note that CDOP is based on a global data set, while our data are regional; and the Wavemill and KaDOP data sets are local. Also, the corrections applied to the different data sets, such as dc calibration and the subtraction of surface currents, are probably responsible for a part of the differences. In CDOP and this work, no subtraction but filtering of images containing known strong currents was done. In the Wavemill and KaDOP experiments, in situ measured current at 2–4 m below the surface for Wavemill [54] and at 10 m for KaDOP [19] were subtracted from the data. The wind data sets used for binning the dc, *in situ* (Wavemill and KaDOP) vs European Centre for Medium-Range Weather Forecasts (ECMWF) reanalysis (CDOP and this work), might contribute to the deviation between the data sets. Finally, differences due to different radar frequencies and resolutions should not be excluded.

Analysis of the dual-polarized data shows that PR is systematically larger than 1 and increases with incidence angle, in agreement with previous studies, e.g., [22], [68]. In addition, we found that the measured PR is significantly smaller than the PR predicted by Bragg scattering theory in both of its forms, pure Bragg and composite surface model. However, the measured PR is most consistent with our empirical fit, followed by the empirical model developed in [57]. Similarly, the dual-polarized data analysis showed that the PD is systematically lower than zero and increases, in absolute value, with incidence angle. This is in agreement with the simulation of the tilt MTF (see Fig. 1) and previous studies, e.g., [17]. It is also found that the measured PD is smaller than the PD predicted by the Bragg scattering theory in both of its forms. The PD calculated using our Doppler model with the tilt MTF derived from the NRCS data is the most consistent with the measured PD, followed by the PD calculated using our Doppler model with the tilt MTF derived from XMOD2. The fact that Bragg scattering theory overestimates both PR and PD (in absolute value), suggests that other scattering mechanisms, e.g., wave breaking, are involved and should be taken into account. The advantage of using empirical models is that they naturally include all scattering effects.

As mentioned earlier, in order to retrieve ocean surface currents from SAR data, a Doppler model is needed to correct for the wave contribution. The wave contribution has, in a previous study [5], been shown to be significant for C-band and in this study we confirm that it is significant also for X-band. Despite major efforts dedicated to developing theory-based models in the last decades, it is found that the investigated theory-based models deviate from each other and from the data, e.g., they overestimate PR and PD. On the other hand, the empirical dc GMFs and the dc models based on empirical MTFs are more consistent with the data.

This motivates the use of empirical models for ocean surface current retrieval following the traditional wind retrieval approach from scatterometers using empirical GMFs. The development of scatterometer GMFs started in the 1980s, while the first Doppler GMF was developed in 2012 [7] and since then there were few validation studies due to the lack of Doppler data. Thus, the development of Doppler GMFs is in its early phase and improvement should continue as more data become available.

Resolving the discrepancies between models will require additional data. We expect that, considering additional TanDEM-X science campaigns or other X-band SAR mission suitable for DCA, more robust Doppler GMF for a range of incidence angles, wind speeds, and wind directions can be built and used for ocean current retrieval. In parallel, theory development will also benefit from extended SAR Doppler data for validation.

Appendix A
Wave-Induced Doppler Model

We start with (10) in [15], in polar coordinates. Assuming that the MTF is identical for the advancing and receding Bragg waves, the equation writes

$$f_D = \overline{f}_B + \Re\left\{\iint D^*(k,\varphi)M(k,\varphi)k^2\Psi(k,\varphi)kdkd\varphi\right\} \quad \text{(A1)}$$

where $\overline{f}_B$ is the weighted mean of the Doppler shift due to Bragg waves propagating toward and away from the radar. $M(k,\varphi)$ is the total MTF, which is the sum of the range, tilt and hydrodynamic MTF ($M = M^r + M^t + M^h$). Note that these are complex quantities. The dependence of M on k and φ is omitted in the following for simplicity. $\Psi(k,\varphi)$ is the 2-D wave height spectrum. $D(k,\varphi)$ is defined as the Doppler MTF in [15]. It is a mapping operator that projects the orbital velocities to the LOS and converts the LOS component to Doppler frequency shift. It is given by

$$D(k,\varphi) = \frac{k_e}{\pi}\frac{\omega(k)}{k}(-\cos\varphi\sin\theta + i\cos\theta) \quad \text{(A2)}$$

where k_e is the electromagnetic wavenumber, θ is the incidence angle, and φ is the propagation direction of the long-waves relative to the range direction (LOS), ω and k are the wave angular frequency and wavenumber, respectively, and i is the imaginary unit.

Replacing D and M in A1, we get

$$\begin{aligned} f_D = \overline{f}_B + \frac{k_e}{\pi} \\ \cdot \Re\left\{\iint \frac{\omega(k)}{k}(-\cos\varphi\ \ \sin\theta + i\cos\theta)\right. \\ \left.\cdot\ \left[M^r + M^t + \left(M_1^h + iM_2^h\right)\right]k^2\Psi(k,\varphi)kdkd\varphi\right\} \end{aligned} \quad \text{(A3)}$$

where M_1^h and M_2^h are the real and imaginary parts of the hydrodynamic MTF.

Taking the real part of the integral, we get

$$\begin{aligned} f_D = \overline{f}_B + \frac{k_e}{\pi} \\ \cdot \iint \frac{\omega(k)}{k}\left[M_1^h\ \cos\varphi\ \sin\theta + M_0^r\ \cos\varphi\ \cos\theta\right. \\ \left. - M_0^t\ \cos\varphi\ \cos\theta + M_2^h\ \cos\theta\right] \\ \cdot k^2\Psi(k,\varphi)kdkd\varphi \end{aligned} \quad \text{(A4)}$$

where $M_0^r = |M^r(\theta,0)|$ and $M_0^t = |M^t(\theta,0)|$.

Rearranging the terms, we get

$$f_D = \overline{f}_B + \frac{k_e}{\pi} \cdot \iint \omega(k) \cdot \left[\left[\left(M_0^r - M_0^t\right) \cos\theta + M_1^h \sin\theta\right] \cdot \cos\varphi + M_2^h \cos\theta\right] k\Psi(k,\varphi) k dk d\varphi. \quad \text{(A5)}$$

If we neglect M^r and M^h, the second term would reduce to $(k_e/\pi) M^t \cos\theta (U_S/2)$. Where U_S is the deep water surface Stokes drift and is defined as [69] $U_S = 2\iint \omega k \Psi(k,\varphi) k dk d\varphi$. If we replace the M^t by its expression given in Appendix B, we get (15) in [70] which was derived using the KA model.

Converting (A5) to radial ground velocity using 1 and rearranging, we get

$$U_{\text{wv}} = \overline{c}_B + \iint \omega(k) k \left[\left[\left(M_0^r - M_0^t\right) \cot\theta + M_1^h\right] \cdot \cos\varphi + M_2^h \cot\theta\right] \Psi(k,\varphi) k dk d\varphi. \quad \text{(A6)}$$

This is the ground-range wave-induced Doppler velocity, where $\overline{c}_B$ is the weighted phase speed of the Bragg waves. The expression of $\overline{c}_B$ is given in [18], [19], and [53] and it is repeated here for completeness

$$\overline{c}_B = c_B \frac{S(\varphi) - S(\varphi+\pi)}{S(\varphi) + S(\varphi+\pi)} \quad \text{(A7)}$$

where c_B is the phase speed of the Bragg waves, $c_B = 0.24$ m/s at X-band and $\theta = 35°$, $S(\varphi)$ is the spreading function of the directional wave spectrum.

If we neglect M^r and we replace $\Psi(k,\varphi)$ by $k^{-4}B(k,\varphi)$ in (A6), where $B(k,\varphi)$ is the wave saturation spectrum, we get (3) and (5) in [16] and [17], respectively.

For a monochromatic sea (Bragg waves + one dominant longwave) with longwave wavenumber k_1, (A6) simplifies to

$$U_{\text{wv}} = \overline{c}_B + \frac{\omega(k_l) k_l A_l^2}{2} \cdot \left[\left[\left(M_0^r - M_0^t\right) \cot\theta + M_1^h(k_l)\right] \cos\varphi + M_2^h(k_1) \cot\theta\right] \quad \text{(A8)}$$

where $\omega(k_l)$, k_l and A_l are the frequency, wavenumber, and amplitude of the dominant longwave, respectively.

If we neglect M^r and replace $\omega(k) k A^2$ by the deep water surface Stokes drift U_S in (A8), we get (50) in [18]. Furthermore, if we consider a range traveling wave ($\varphi = 0$), we get (B16) in [5] without the current term. The multiplicative term $\omega k A^2$ can also be written in the standard wave parameters H_s (significant wave height) and T_p (peak wave period), as $(\pi/T_p)^3 \, g^{-1} H_s^2$, where g is the acceleration due to gravity.

Note that different authors adopt different conventions for φ. In this article, $\varphi = 0$ corresponds to the upwave and upwind. There are also different conventions for the phase of the MTF, here we follow [21], [26]. That is, a phase of 0 means that maximum backscatter occurs at the crest and a positive phase means that it occurs at the forward face of the wave.

Appendix B
Tilt MTF

We start with (6) and (7) in [39] and divide by $|k|$ to get the dimensionless tilt MTF

$$M^t = i \frac{1}{\sigma^0} \left[\frac{\partial\sigma}{\partial\zeta_x} \frac{k_\parallel}{|k|} + \frac{\partial\sigma}{\partial\zeta_y} \frac{k_\perp}{|k|}\right] \quad \text{(B1)}$$

where $k_\parallel$ and $k_\perp$ are the wave vector components of the longwave parallel and perpendicular to the radar LOS. ζ_x and ζ_y are the slopes parallel and perpendicular to the plane of incidence, respectively.

Introducing φ the angle between the longwave propagation and the radar LOS direction, we get

$$M^t = i \frac{1}{\sigma^0} \left[\frac{\partial\sigma}{\partial\zeta_x} \cos\varphi + \frac{\partial\sigma}{\partial\zeta_y} \sin\varphi\right]. \quad \text{(B2)}$$

The parallel slope variation can be approximated (for small slopes) by [26] $\partial\zeta_x = -\partial \tan\theta \approx -\partial\theta$, and the perpendicular slope can be approximated by [25] $\partial\zeta_y = -\tan\theta \partial\varphi$, where θ is the incidence angle.

Replacing $\partial\zeta_x$ and $\partial\zeta_y$, by their approximations, into (B2), we get the 2-D tilt MTF

$$M^t(\theta,\varphi) = -i \frac{1}{\sigma^0} \left[\frac{\partial\sigma}{\partial\theta} \cos\varphi + \frac{1}{\tan\theta} \frac{\partial\sigma}{\partial\varphi} \sin\varphi\right]. \quad \text{(B3)}$$

The second term in B3 is very small compared to the first term at moderate incidence angles ($\theta > 20°$), so it is often neglected.

Appendix C
Hydrodynamic MTF

We start from (B15) in [28] [or (8) in [39]], and divide by $|k_l|$ to get the dimensionless MTF

$$M^h = \frac{\omega - i\beta}{\omega^2 + \beta^2} \frac{\omega}{|k_l|^2} (k \cdot k_l) \left[\frac{k_l}{\Psi} \frac{\partial\Psi}{\partial k} - \gamma \frac{k \cdot k_l}{|k|^2}\right] \quad \text{(C1)}$$

where k and k_l are the short (Bragg) and the long wave vectors, respectively. $\gamma = c_g/c_B$, where c_g and c_B are the group and phase velocity of the Bragg wave, respectively, ω is the angular frequency of the long modulating wave, and β is the relaxation rate.

Introducing φ, the angle between the long wave and the Bragg wave, we obtain

$$M^h = \frac{\omega^2 - i\omega\beta}{\omega^2 + \beta^2} \cos\varphi \left[\frac{|k|}{|k_l|} \frac{k_l}{\Psi} \frac{\partial\Psi}{\partial k} - \gamma \cos\varphi\right]. \quad \text{(C2)}$$

Rearranging the terms, we obtain

$$M^h = \frac{\omega^2 - i\omega\beta}{\omega^2 + \beta^2} \cos\varphi \left[\frac{|k|}{\Psi} \cos\varphi \frac{\partial\Psi}{\partial|k|} + \frac{1}{\Psi} \sin\varphi \frac{\partial\Psi}{\partial\varphi} - \gamma \cos\varphi\right]. \quad \text{(C3)}$$

Following [21], we change the sign of the real part to keep the phase convention (0 at the crest and positive on the forward face). This does not change the magnitude but shifts the phase by π.

After the sign change and terms rearranging, we obtain

$$M^h = -\frac{\omega^2 + i\beta\ \omega}{\omega^2 + \beta^2} \cdot \left[\cos^2\varphi\left(\frac{k}{\Psi}\frac{\partial\Psi}{\partial k} - \gamma\right) + \cos\varphi\sin\varphi\frac{1}{\Psi}\frac{\partial\Psi}{\partial\varphi}\right]. \quad \text{(C4)}$$

In the above notation, we have omitted the dependence of ω on k and the dependence of Ψ on k and φ. Note that the second term in C4 vanishes in the parallel direction, and the whole M^h vanishes when the modulating wave is perpendicular to the Bragg wave.

If we use a Phillips like [45] form for the wave spectrum

$$\Psi(k,\varphi) = \Psi(k,0)\cdot S(\varphi) = \alpha|k|^{-4}\,\mathrm{sech}(\varphi)^2 \quad \text{(C5)}$$

where $S(\varphi)$ is the spreading function and α is a constant. In a more complete spectrum, Ψ should depend also on wind speed and S should depend on k and wind speed.

Substituting (C5) into (C4) and using $c_B = 2c_g$ hence $\gamma = 0.5$, for gravity waves, we obtain the 2-D hydrodynamic MTF

$$M^h(k,\varphi) = \frac{\omega^2 + i\beta\ \omega}{\omega^2 + \beta^2}\cdot\left[4.5\cos^2\varphi + 2\sin\varphi\cos\varphi\tanh\varphi\right]. \quad \text{(C6)}$$

The expression for the hydrodynamic MTF including the wave breaking effect is given in [31], (19)–(23).

Appendix D
Tilt MTF for the Bragg and Composite Models

According to the pure Bragg scattering theory [36], the normalized radar cross section (NRCS or σ^0) of the ocean surface is expressed as

$$\sigma_B^0(\theta,\varphi) = 16\pi k_e^4\cos^4\theta|G_{pp}(\theta,\epsilon_r)|^2\Psi(k_B,\varphi) \quad \text{(D1)}$$

where G_{pp} is the scattering coefficient. It depends on the incidence angle θ, polarization pp (HH or VV) and the complex dielectric constant ϵ_r.

If replace the wave spectrum by the Phillips spectrum at the Bragg wavenumber in D1, we get

$$\sigma_B^0(\theta,\varphi) = \pi\ \cos(\theta)^4|G_{pp}(\theta,\epsilon_r)|^2\sin(\theta)^{-4} \quad \text{(D2)}$$

where $\epsilon_r = 54.5$ - i 37 is the complex dielectric constant, calculated from the double-Debye model in [71] for X-band ($f_e = 9.65$ GHz), temperature 16^o Celsius and salinity 32 psu.

We use the composite model expression in [[22], (31)], without the hydrodynamic term, i.e., the third term in their (31) is neglected

$$\sigma_c^0(\theta,\varphi) = \sigma_B^0(\theta,\varphi)\left(1 + g_{pp}\overline{\zeta_i^2}\right) \quad \text{(D3)}$$

where $\overline{\zeta_i^2}$ is the mean square slope of the tilting waves and g_{vv} and g_{hh} are given in (32) and (33) in [22], respectively.

Apply B3, without the second term, we obtain tilt MTF for the composite model as

$$M_{pp}^t = -i\left[\frac{1}{|G_t|^2}\frac{\partial|G_t|^2}{\partial\theta} + \frac{\overline{\zeta_i^2}}{\left(1 + g_{pp}\overline{\zeta_i^2}\right)}\frac{\partial g_{pp}}{\partial\theta}\right]\cos\varphi \quad \text{(D4)}$$

where $|G_t|^2 = |G_{pp}|^2\cos(\theta)^2\sin(\theta)^{-4}$. The first term in D4 is the pure Bragg tilt MTF.

Acknowledgment

TanDEM-X data were provided by the German Aerospace Center (DLR) under the license agreement ATI OCEA0401. Wind and wave data were provided by the European Centre for Medium-Range Weather Forecasts (ECMWF). The authors would like to thank DLR and ECMWF.

References

[1] J. Horstmann and W. Koch, "Measurement of ocean surface winds using synthetic aperture radars," *IEEE J. Ocean. Eng.*, vol. 30, no. 3, pp. 508–515, Jul. 2005.

[2] G. Engen, H. Johnsen, H. E. Krogstad, and S. F. Barstow, "Directional wave spectra by inversion of ERS-1 synthetic aperture radar ocean imagery," *IEEE Trans. Geosci. Remote Sens.*, vol. 32, no. 2, pp. 340–352, Mar. 1994.

[3] R. M. Goldstein and H. A. Zebker, "Interferometric radar measurement of ocean surface currents," *Nature*, vol. 328, no. 6132, pp. 707–709, Aug. 1987.

[4] D. R. Thompson and J. R. Jensen, "Synthetic aperture radar interferometry applied to ship generated internal waves in the 1989 Loch Linnhe experiment," *J. Geophys. Res., Oceans*, vol. 98, no. C6, pp. 10259–10269, 1993.

[5] B. Chapron, F. Collard, and F. Ardhuin, "Direct measurements of ocean surface velocity from space: Interpretation and validation," *J. Geophys. Res., Oceans*, vol. 110, no. C7, 2005. [Online]. Available: https://agupubs.onlinelibrary.wiley.com/doi/abs/10.1029/2004JC002809, doi: 10.1029/2004JC002809.

[6] F. Collard, A. A. Mouche, B. Chapron, C. Danilo, and J. Johannessen, "Routine high resolution observation of selected major surface currents from space," in *Proc. Adv. SAR Oceanogr. ENVISAT ERS Missions (SEASAR)*, ESA Special Publication, vol. 676, Jan. 2008, p. 5.

[7] A. A. Mouche *et al.*, "On the use of Doppler shift for sea surface wind retrieval from SAR," *IEEE Trans. Geosci. Remote Sens.*, vol. 50, no. 7, pp. 2901–2909, Jul. 2012.

[8] A. Elyouncha, L. E. B. Eriksson, R. Romeiser, and L. M. H. Ulander, "Measurements of sea surface currents in the baltic sea region using spaceborne along-track InSAR," *IEEE Trans. Geosci. Remote Sens.*, vol. 57, no. 11, pp. 8584–8599, Nov. 2019.

[9] J. V. Toporkov and G. S. Brown, "Numerical simulations of scattering from time-varying, randomly rough surfaces," *IEEE Trans. Geosci. Remote Sens.*, vol. 38, no. 4, pp. 1616–1625, Jul. 2000.

[10] D. R. Thompson, "Calculation of microwave Doppler spectra from the ocean surface with a time-dependent composite model," in *Radar Scattering from Modulated Wind Waves*. Dordrecht, The Netherlands: Springer, May 1989, pp. 27–40.

[11] A. A. Mouche, B. Chapron, N. Reul, and F. Collard, "Predicted Doppler shifts induced by ocean surface wave displacements using asymptotic electromagnetic wave scattering theories," *Waves Random Complex Media*, vol. 18, no. 1, pp. 185–196, Jan. 2008.

[12] F. Nouguier, C.-A. Guerin, and G. Soriano, "Analytical techniques for the Doppler signature of sea surfaces in the microwave regime—II: Nonlinear surfaces," *IEEE Trans. Geosci. Remote Sens.*, vol. 49, no. 12, pp. 4920–4927, Dec. 2011.

[13] F. Fois, P. Hoogeboom, F. Le Chevalier, and A. Stoffelen, "An analytical model for the description of the full-polarimetric sea surface Doppler signature," *J. Geophys. Res., Oceans*, vol. 120, no. 2, pp. 988–1015, Feb. 2015.

[14] W. J. Plant, "The modulation transfer function: Concept and applications," in *Radar Scattering from Modulated Wind Waves*. Dordrecht, The Netherlands: Springer, 1989, pp. 155–172.

[15] R. Romeiser and D. R. Thompson, "Numerical study on the along-track interferometric radar imaging mechanism of oceanic surface currents," *IEEE Trans. Geosci. Remote Sens.*, vol. 38, no. 1, pp. 446–458, Jan. 2000.

[16] J. A. Johannessen *et al.*, "Direct ocean surface velocity measurements from space: Improved quantitative interpretation of ENVISAT ASAR observations," *Geophys. Res. Lett.*, vol. 35, no. 22, 2008.

[17] M. W. Hansen *et al.*, "Simulation of radar backscatter and Doppler shifts of wave–current interaction in the presence of strong tidal current," *Remote Sens. Environ.*, vol. 120, pp. 113–122, May 2012.

[18] E. Rodríguez *et al.*, "Estimating ocean vector winds and currents using a Ka-band pencil-beam Doppler scatterometer," *Remote Sens.*, vol. 10, no. 4, p. 576, Apr. 2018.

[19] Y. Yurovsky, V. Kudryavtsev, S. Grodsky, and B. Chapron, "Sea surface Ka-band Doppler measurements: Analysis and model development," *Remote Sens.*, vol. 11, no. 7, p. 839, Apr. 2019.

[20] J. V. Toporkov, M. A. Sletten, and G. S. Brown, "Numerical scattering simulations from time-evolving ocean-like surfaces at L- and X-band : Doppler analysis and comparisons with a composite surface analytical model," in *Proc. 27th URSI Gen. Assem.*, Maastricht, The Netherlands, 2002.

[21] R. Romeiser, W. Alpers, and V. Wismann, "An improved composite surface model for the radar backscattering cross section of the ocean surface: 1. Theory of the model and optimization/validation by scatterometer data," *J. Geophys. Res., Oceans*, vol. 102, no. C11, pp. 25237–25250, Nov. 1997.

[22] V. Kudryavtsev, "A semiempirical model of the normalized radar cross-section of the sea surface 1. Background model," *J. Geophys. Res.*, vol. 108, no. C3, pp. 1–24, 2003.

[23] J. W. Wright, W. J. Plant, W. C. Keller, and W. L. Jones, "Ocean wave-radar modulation transfer functions from the West Coast Experiment," *J. Geophys. Res., Oceans*, vol. 85, no. C9, pp. 4957–4966, 1980.

[24] J. Schröter, F. Feindt, W. Alpers, and W. C. Keller, "Measurement of the ocean wave-radar modulation transfer function at 4.3 GHz," *J. Geophys. Res., Oceans*, vol. 91, no. C1, pp. 923–932, 1986.

[25] T. Hara and W. J. Plant, "Hydrodynamic modulation of short wind-wave spectra by long waves and its measurement using microwave backscatter," *J. Geophys. Res., Oceans*, vol. 99, no. C5, pp. 9767–9784, 1994.

[26] R. Romeiser, A. Schmidt, and W. Alpers, "A three-scale composite surface model for the ocean wave–radar modulation transfer function," *J. Geophys. Res., Oceans*, vol. 99, no. C5, pp. 9785–9801, 1994.

[27] W. C. Keller and J. W. Wright, "Microwave scattering and the straining of wind-generated waves," *Radio Sci.*, vol. 10, no. 2, pp. 139–147, Feb. 1975.

[28] W. Alpers and K. Hasselmann, "The two-frequency microwave technique for measuring ocean-wave spectra from an airplane or satellite," *Boundary-Layer Meteorol.*, vol. 13, nos. 1–4, pp. 215–230, Jan. 1978.

[29] D. P. Kasilingam and O. H. Shemdin, "The validity of the composite surface model and its applications to the modulation of radar backscatter," *Int. J. Remote Sens.*, vol. 13, no. 11, pp. 2079–2104, Jul. 1992.

[30] W. J. Plant, "A model for microwave Doppler sea return at high incidence angles: Bragg scattering from bound, tilted waves," *J. Geophys. Res., Oceans*, vol. 102, no. C9, pp. 21131–21146, 1997.

[31] V. Kudryavtsev, "A semiempirical model of the normalized radar cross section of the sea surface, 2. Radar modulation transfer function," *J. Geophys. Res.*, vol. 108, no. C3, pp. 1–16, 2003.

[32] K. Miller and M. Rochwarger, "A covariance approach to spectral moment estimation," *IEEE Trans. Inf. Theory*, vol. 18, no. 5, pp. 588–596, Sep. 1972.

[33] M. W. Hansen, F. Collard, K.-F. Dagestad, J. A. Johannessen, P. Fabry, and B. Chapron, "Retrieval of sea surface range velocities from ENVISAT ASAR Doppler centroid measurements," *IEEE Trans. Geosci. Remote Sens.*, vol. 49, no. 10, pp. 3582–3592, Oct. 2011.

[34] S. Duque, "TanDEM-X payload ground segment–CoSSC generation and interferometric considerations," German Aerosp. Center (DLR), Weßling, Germany, Tech. Rep. TD-PGS-TN-3129, May 2012.

[35] H. C. Graber, D. R. Thompson, and R. E. Carande, "Ocean surface features and currents measured with synthetic aperture radar interferometry and HF radar," *J. Geophys. Res., Oceans*, vol. 101, no. C11, pp. 25813–25832, Nov. 1996.

[36] J. Wright, "Backscattering from capillary waves with application to sea clutter," *IEEE Trans. Antennas Propag.*, vol. 14, no. 6, pp. 749–754, Nov. 1966.

[37] G. R. Valenzuela, "Theories for the interaction of electromagnetic and oceanic waves? A review," *Boundary-Layer Meteorol.*, vol. 13, nos. 1–4, pp. 61–85, Jan. 1978.

[38] J. Wright, "A new model for sea clutter," *IEEE Trans. Antennas Propag.*, vol. 16, no. 2, pp. 217–223, Mar. 1968.

[39] W. Alpers, D. B. Ross, and C. L. Rufenach, "On the detectability of ocean surface waves by real and synthetic aperture radar," *J. Geophys. Res.*, vol. 86, no. C7, pp. 6481–6498, 1981.

[40] W. C. Keller, W. J. Plant, R. A. Petitt, and E. A. Terray, "Microwave backscatter from the sea: Modulation of received power and Doppler bandwidth by long waves," *J. Geophys. Res.*, vol. 99, no. C5, p. 9751, 1994.

[41] M. A. Donelan, B. K. Haus, W. J. Plant, and O. Troianowski, "Modulation of short wind waves by long waves," *J. Geophys. Res., Oceans*, vol. 115, no. C10, 2010. [Online]. Available: https://agupubs.onlinelibrary.wiley.com/doi/abs/10.1029/2009JC005794, doi: 10.1029/2009JC005794.

[42] F. Feindt, J. Schröter, and W. Alpers, "Measurement of the ocean wave-radar modulation transfer function at 35 GHz from a sea-based platform in the North Sea," *J. Geophys. Res., Oceans*, vol. 91, no. C8, pp. 9701–9708, 1986.

[43] Y. Y. Yurovsky, V. N. Kudryavtsev, B. Chapron, and S. A. Grodsky, "Modulation of Ka-band Doppler radar signals backscattered from the sea surface," *IEEE Trans. Geosci. Remote Sens.*, vol. 56, no. 5, pp. 2931–2948, May 2018.

[44] J. F. R. Gower, "'Layover' in satellite radar images of ocean waves," *J. Geophys. Res., Oceans*, vol. 88, no. C12, pp. 7719–7720, 1983.

[45] O. M. Phillips, "The equilibrium range in the spectrum of wind-generated waves," *J. Fluid Mech.*, vol. 4, no. 04, p. 426–436, Aug. 1958.

[46] X.-M. Li and S. Lehner, "Algorithm for sea surface wind retrieval from TerraSAR-X and TanDEM-X data," *IEEE Trans. Geosci. Remote Sens.*, vol. 52, no. 5, pp. 2928–2938, May 2014.

[47] H. Hersbach, A. Stoffelen, and S. de Haan, "An improved C-band scatterometer ocean geophysical model function: CMOD5," *J. Geophys. Res.*, vol. 112, no. C3, 2007.

[48] K. Hasselmann and S. Hasselmann, "On the nonlinear mapping of an ocean wave spectrum into a synthetic aperture radar image spectrum and its inversion," *J. Geophys. Res.*, vol. 96, no. C6, pp. 10713–10729, 1991.

[49] E. A. Caponi, D. R. Crawford, H. C. Yuen, and P. G. Saffman, "Modulation of radar backscatter from the ocean by a variable surface current," *J. Geophys. Res., Oceans*, vol. 93, no. C10, pp. 12249–12263, 1988.

[50] W. J. Plant, "A relationship between wind stress and wave slope," *J. Geophys. Res.-Oceans*, vol. 87, no. Nc3, pp. 1961–1967, 1982.

[51] A. Schmidt, V. Wismann, R. Romeiser, and W. Alpers, "Simultaneous measurements of the ocean wave—Radar modulation transfer function at L, C, and X bands from the research platform Nordsee," *J. Geophys. Res., Oceans*, vol. 100, no. C5, pp. 8815–8827, 1995.

[52] F. Ardhuin *et al.*, "Measuring currents, ice drift, and waves from space: The sea surface Kinematics multiscale monitoring (SKIM) concept," *Ocean Sci.*, vol. 14, no. 3, pp. 337–354, May 2018.

[53] D. Moller, S. J. Frasier, D. L. Porter, and R. E. McIntosh, "Radar-derived interferometric surface currents and their relationship to subsurface current structure," *J. Geophys. Res., Oceans*, vol. 103, no. C6, pp. 12839–12852, Jun. 1998.

[54] A. C. H. Martin, C. Gommenginger, J. Marquez, S. Doody, V. Navarro, and C. Buck, "Wind-wave-induced velocity in ATI SAR ocean surface currents: First experimental evidence from an airborne campaign," *J. Geophys. Res., Oceans*, vol. 121, no. 3, pp. 1640–1653, Mar. 2016.

[55] J. Wu, "Sea-surface drift currents induced by wind and waves," *J. Phys. Oceanogr.*, vol. 13, no. 8, pp. 1441–1451, Aug. 1983.

[56] F. Ardhuin, L. Marié, N. Rascle, P. Forget, and A. Roland, "Observation and estimation of Lagrangian, Stokes, and eulerian currents induced by wind and waves at the sea surface," *J. Phys. Oceanogr.*, vol. 39, no. 11, pp. 2820–2838, Nov. 2009.

[57] A. A. Mouche, D. Hauser, J.-F. Daloze, and C. Guerin, "Dual-polarization measurements at C-band over the ocean: Results from airborne radar observations and comparison with ENVISAT ASAR data," *IEEE Trans. Geosci. Remote Sens.*, vol. 43, no. 4, pp. 753–769, Apr. 2005.

[58] W. Shao, Z. Zhang, X. Li, and W. Wang, "Sea surface wind speed retrieval from TerraSAR-X HH polarization data using an improved polarization ratio model," *IEEE J. Sel. Topics Appl. Earth Observ. Remote Sens.*, vol. 9, no. 11, pp. 4991–4997, Nov. 2016.

[59] G. Krieger *et al.*, "TanDEM-X: A satellite formation for high-resolution SAR interferometry," *IEEE Trans. Geosci. Remote Sens.*, vol. 45, no. 11, pp. 3317–3341, Nov. 2007.

[60] S. Suchandt and R. Romeiser, "X-band sea surface coherence time inferred from bistatic SAR interferometry," *IEEE Trans. Geosci. Remote Sens.*, vol. 55, no. 7, pp. 3941–3948, Jul. 2017.

[61] R. Romeiser, H. Runge, S. Suchandt, R. Kahle, C. Rossi, and P. S. Bell, "Quality assessment of surface current fields from TerraSAR-X and TanDEM-X along-track interferometry and Doppler centroid analysis," *IEEE Trans. Geosci. Remote Sens.*, vol. 52, no. 5, pp. 2759–2772, May 2014.

[62] T. Fritz, M. Eineder, and J. Mittermayer, "TerraSAR-X ground segment—Basic product specification document," German Aerosp. Center (DLR), Weßling, Germany, Tech. Rep. TX-GS-DD-3302, Oct. 2013.
[63] H. Hersbach *et al.*, "Meteorology," in *Global Reanalysis: Goodbye ERA-Interim, Hello ERA5*, no. 159. Apr. 2019, pp. 17–24. [Online]. Available: https://www.ecmwf.int/node/19027, doi: 10.21957/vf291hehd7.
[64] M.-H. Rio, S. Mulet, and N. Picot, "Beyond GOCE for the ocean circulation estimate: Synergetic use of altimetry, gravimetry, and *in situ* data provides new insight into geostrophic and ekman currents," *Geophys. Res. Lett.*, vol. 41, no. 24, pp. 8918–8925, Dec. 2014.
[65] A. A. Mouche, D. Hauser, and V. Kudryavtsev, "Radar scattering of the ocean surface and sea-roughness properties: A combined analysis from dual-polarizations airborne radar observations and models in C band," *J. Geophys. Res., Oceans*, vol. 111, no. C9, 2006. [Online]. Available: https://agupubs.onlinelibrary.wiley.com/doi/abs/10.1029/2005JC003166, doi: 10.1029/2005JC003166.
[66] V. N. Kudryavtsev, B. Chapron, A. G. Myasoedov, F. Collard, and J. A. Johannessen, "On dual co-polarized SAR measurements of the ocean surface," *IEEE Geosci. Remote Sens. Lett.*, vol. 10, no. 4, pp. 761–765, Jul. 2013.
[67] V. Kudryavtsev, I. Kozlov, B. Chapron, and J. A. Johannessen, "Quad-polarization SAR features of ocean currents," *J. Geophys. Res., Oceans*, vol. 119, no. 9, pp. 6046–6065, Sep. 2014.
[68] Y. Y. Yurovsky, V. N. Kudryavtsev, S. A. Grodsky, and B. Chapron, "Ka-band dual copolarized empirical model for the sea surface radar cross section," *IEEE Trans. Geosci. Remote Sens.*, vol. 55, no. 3, pp. 1629–1647, Mar. 2017.
[69] K. E. Kenyon, "Stokes drift for random gravity waves," *J. Geophys. Res.*, vol. 74, no. 28, pp. 6991–6994, Dec. 1969.
[70] F. Nouguier *et al.*, "Sea surface kinematics from near-nadir radar measurements," *IEEE Trans. Geosci. Remote Sens.*, vol. 56, no. 10, pp. 6169–6179, Oct. 2018.
[71] F. T. Ulaby and D. G. Long, *Microwave Radar and Radiometric Remote Sensing*, 1st ed. Ann Arbor, MI, USA: Univ. Michigan, 2014.

Anis Elyouncha (Member, IEEE) received the B.S. degree in electrical engineering from the Institut Superieur Industriel de Bruxelles, Brussels, Belgium, in 2004, the M.S. degree in electrical engineering and telecommunications from the Universite Libre de Bruxelles, Brussels, in 2006, and the Ph.D. degree in radio and space sciences from Chalmers University of Technology, Gothenburg, Sweden, in 2020.

From 2008 to 2015, he was a Research Engineer with the Royal Military Academy of Belgium, Brussels. He is a Postdoc Researcher with the Department of Space, Earth and Environment, Chalmers University of Technology. His research interests include ocean parameters retrieval from SAR data, electromagnetic scattering from the sea surface, and radar signal processing.

Leif E. B. Eriksson (Member, IEEE) received the University Certificate in space technology from Umeå University, Umeå, Sweden, in 1993, the M.S. degree in electrical engineering from the Chalmers University of Technology, Gothenburg, Sweden, in 1998, and the Ph.D. degree from Friedrich-Schiller University, Jena, Germany, in 2004.

From 1999 to 2000, he was employed by the Joint Research Centre of the European Commission with the Space Application Institute in Ispra, Ispra, Italy. From 2000 to 2004, he was with the Department of Geoinformatics, Friedrich-Schiller University. In 2004, he joined the radar remote sensing group with the Chalmers University of Technology, where he holding a position as an Associate Professor of radar remote sensing, since 2012. He is with the Department of Space, Earth and Environment, Chalmers University of Technology. His research interest includes the use of SAR to retrieve information about ocean, sea ice, and forest.

Roland Romeiser (Senior Member, IEEE) received the Dipl.-Phys. degree from the University of Bremen, Bremen, Germany, in 1990, and the Dr.rer.nat. and Habilitation degrees from the University of Hamburg, Hamburg, Germany, in 1993 and 2007, respectively.

From 1990 to 2008, he was with the Institute of Oceanography, University of Hamburg. From August 1998 to July 1999, he spent a year with the Applied Physics Laboratory, Johns Hopkins University, Laurel, MD, USA, as a Feodor Lynen Fellow of the Alexander von Humboldt Foundation. In April 2008, he joined the Rosenstiel School of Marine and Atmospheric Science of the University of Miami, Miami, FL, USA, where he is currently a full Professor. He has wide experience in the field of remote sensing of ocean currents, waves, and winds by airborne and spaceborne microwave radars. Most of his recent research has focused on advanced synthetic aperture radar (SAR) processing and algorithm development for current and wave retrievals.

Dr. Romeiser was an Associate Editor of the IEEE JOURNAL OF OCEANIC ENGINEERING from 2000 to 2020 and of the IEEE TRANSACTIONS ON GEOSCIENCE AND REMOTE SENSING from 2014 to 2017.

Lars M. H. Ulander (Fellow, IEEE) received the M.Sc. degree in engineering physics and the Ph.D. degree in electrical and computer engineering from Chalmers University of Technology, Gothenburg, Sweden, in 1985 and 1991, respectively.

Since 2014, he has been a Professor of radar remote sensing with the Chalmers University of Technology. He also holds a part-time position with the Swedish Defence Research Agency (FOI), Linköping, Sweden, where he is the Director of Research in radar signal processing and leads the research on VHF/UHF-band radar. He has authored or coauthored over 300 professional publications, of which more than 80 are in peer-reviewed scientific journals. His research areas include radar imaging, synthetic aperture radar (SAR), signal processing, electromagnetic scattering models, and remote sensing applications.